PROCEEDINGS

OF 12TH INTERNATIONAL CONFERENCE ON COMMUNICATIONS, ELECTROMAGNETICS AND MEDICAL APPLICATIONS (CEMA'17)

Organized by:

FACULTY OF TELECOMMUNICATIONS
TECHNICAL UNIVERSITY OF SOFIA, BULGARIA

NATIONAL TECHNICAL UNIVERSITY OF ATHENS, GREECE,
SCHOOL OF ELECTRICAL AND COMPUTER ENGINEERING

NATIONAL TECHNICAL UNIVERSITY OF ATHENS, GREECE

SCHOOL OF ELECTRICAL AND COMPUTER ENGINEERING

Sofia, Bulgaria
12th – 14th October, 2017

KING 2001, Sofia

Edited by Prof. Dr. Eng. **Dimiter Tz. Dimitrov**

ISSN: 1314-2100
SCOPUS tracking nr.6B4F77263D276412
Printed in Bulgaria
KING 2001, Sofia

P. Frangos

D. Dimitrov

K. Dimitrov

Dear Colleagues,

It is our privilege to thank all of you for your contributions submitted at 12th regular International Conference on 'Communication, Electromagnetic and Medical Applications' CEMA'17. This is a conference which should help future collaboration in the area of engineering, especially in the area of communication technologies and medical applications. This is an important scientific event not only in Balkan region, but in Europe, also. The International Conference on Communication, Electromagnetism and Medical Applications CEMA'17 is dedicated to all essential aspects of the development of global information and communication technologies, and their impact in medicine, as well. The objective of Conference is to bring together lecturers, researchers and practitioners from different countries, working on the field of communication, electromagnetism, medical applications and computer simulation of electromagnetic field, in order to exchange information and bring new contribution to this important field of engineering design and application in medicine. The Conference will bring you the latest ideas and development of the tools for the above mentioned scientific areas directly from their inventors. The objective of the Conference is also to bring together the academic community, researchers and practitioners working in the field of Communication, Electromagnetic and Medical Applications, not only from all over Europe, but also from America and Asia, in order to exchange information and present new scientific and technical contributions.

Many well known scientists took part in conference preparation as members of International Scientific Committee or/and as reviewers of submitted papers. We would like to thank all of them for their efforts, for their suggestions and advices.

We are extremely grateful to the company INTRACOM Bulgaria for its regular support of our conference.

On behalf of the International Scientific Committee, we would like to wish you successful presentations of your papers, successful discussions and new collaborations for your future scientific investigations.

Engineering and medicine should provide high level of living for all people.

D. Dimitrov
Conference Chairman

P. Frangos
Conference Vice Chairman

K. Dimitrov
Conference Vice Chairman

INTERNATIONAL SCIENTIFIC COMMITTEE

Chairman:

D. TZ. DIMITROV, Technical University of Sofia, Bulgaria

Vice Chairmen:

P. FRANGOS, National Technical University of Athens, Greece
K. L. DIMITROV, Technical University of Sofia, Bulgaria

Members:

N. AMPILOVA,	University of Petersburg, Russia
D. ANDRIUKAITIS,	Kaunas University of Technology, Lithuania
T. AOYAGI,	Tokyo Institute of Technology, Japan
A. BEKJARSKY,	Technical University of Sofia, Bulgaria
R. BRUZGIENE,	Kaunas University of Technology, Lithuania
M. DONTSCHEWA,	University of Applied Sciences, Dorbirn, Austria
N. ESCUDEIRO,	Inst. Sup. de Engenharia do Porto, Portugal
E. GAGO-RIBAS,	University of Oviedo, Spain
V.GEORGIEVA,	Technical University of Sofia, Bulgaria
S. Ver HOEYE,	University of Oviedo, Spain
M. HOFMANN,	University of Ulm, Germany
I. ILIEV,	Technical University of Sofia, Bulgaria
L. JORDANOVA,	Technical University of Sofia, Bulgaria
G. S. KLIROS,	Hellenic Air-Force Academy, Greece
R. KRIVICKAS,	Kaunas University of Technology, Lithuania
V. KUKENSKA,	Technical University of Gabrovo, Bulgaria
G. MALLET,	University “Sophia Antipolis”, Nice, France
G. MATSOPOULOS,	National Technical University of Athens, Greece
M. MARTINS,	Instituto Superior Técnico, Lisboa, Portugal
M. GONZALEZ-MORALES,	University of Valladolid, Spain
L. NARBUTAITE,	Kaunas University of Technology, Lithuania
K. NIKITA,	National Technical University of Athens, Greece
M. NIKOLOVA,	High Naval School, Varna, Bulgaria
J. PETROVSKA,	Medical University of Sofia, Bulgaria
F. PRATO,	University of Western Ontario, Canada
H. ROTH,	University of Siegen, Germany
S. SAUTBEKOV,	Euroasian University, Astana, Kazakhstan
A. SAVOV,	Medical University of Sofia, Bulgaria
S. SAVOV,	Technical University of Varna, Bulgaria
H-P. SCHADE,	Technical University of Ilmenau, Germany
J. SEBASTIAN,	Universidad Complutense de Madrid, Spain
L. SONG,	Technical University of Harbin, China
A. USHEVA,	University of Boston, USA

REVIEWERS

BALZANO, Q.	University of Maryland, USA
BEHARI, J.	Jawaharlal Nehru University ,New Delhi, India
BERG, H.	Technical University of Jena, Germany
BOEMO, E.	Technical University of Madrid, Spain
DIMITROV, D.	Technical University of Sofia, Bulgaria
DONTSCHEWA, M.	University of Applied Sciences, Dorbirn, Austria
GOUSSETIS, G.	Heriot - Watt University, United Kingdom
MALLET, G.	University "Sophia Antipolis", Nice, France
MARINKEV, V.	Medical University of Plovdiv, Bulgaria
PETROVSKA, J.	Medical University of Sofia, Bulgaria
PRATO, F.	University of Western Ontario, Canada
ROTH, H.	University of Siegen, Germany
SAVOV, A.	Medical University of Sofia, Bulgaria
SCHADE, H-P.	Technical University of Ilmenau, Germany
SONG, L.	Technical University of Harbin, China
USHEVA, A.	University of Boston, USA

REGISTRATION

October, 12th, 09h – 16h
Building of Library, fourth floor
Technical University of Sofia, Bulgaria

CONFERENCE PROGRAM

12th October

OPENING CEREMONY

9h 30min – 10h
Building of Library, fourth floor
Technical University of Sofia, Bulgaria

Coffe Break

10h – 10h 30min

SCIENTIFIC PROGRAM

12th October

FIRST SESSION

10h 30min – 12h
Building of Library, fourth floor
Technical University of Sofia, Bulgaria

Chairman: Prof. Rasa Bruzgiene, Kaunas University of Technology, Lithuania

---

1. **AN APPROACH FOR COLORECTAL POLYP SEGMENTATTION,**
   Veska Georgieva, Plamen Petrov, Technical University of Sofia, Bulgaria

2. **3D VISUALISATION OF THE SPLEEN FROM MRI SEQUENCES,**
   Antonia Mihaylova, Technical University of Sofia, Bulgaria

3. **FRACTAL ANALYSIS METHODS IN INVESTIGATION OF ULTRALIW DOSES EFFECTS,**
   Nataly Ampilova, Igor Soloviev, St. Petersburg State University, St. Petersburg, Russia

4. **USER ACTIVITY RECOGNITION IN AUTOMATED CONTROL OF SMART ENVIRONMENT,**
   Artem Kirienko, St. Petersburg State University, St. Petersburg, Russia

5. **PREPROCESSING AND CLUSTERING RAW ACCELEROMETER DATA FROM SMARTPHONES FOR HUMAN ACTIVITY RECOGNITION,**
   Pavel Dinev, Ivo R. Draganov, Ognian L. Boumbarov , Technical University of Sofia, Bulgaria, Darko Brodić, University of Belgrade, Serbia

Lunch

12h – 13h 30min

SECOND SESSION

13h 30min – 15h
Building of Library, fourth floor
Technical University of Sofia, Bulgaria

Chairman: Prof. N. Ampilova, St. Petersburg State University, St. Petersburg, Russia

1. **EM EXPOSURE STUDY OF A HUMAN INSIDE THE CAR,**
   Veriko Jeladze, Tamar Nozadze, Vasil Tabatadze, Ivan Petoev, Revaz Zaridze, Tbilisi State University, Tbilisi, Georgia

2. **THE EFFECT OF WEATHER ON QUALITY OF EXPERIENCE IN OPTICAL WIRELESS COMMUNICATION SYSTEM,**
   Rasa Bruzgiene, Lina Narbutaite, Kaunas University of Technology, Lithuania, Erich Leitgeb, Pirmin Pezzei, Thomas Plank, Graz University of Technology, Graz, Austria

3. **PHASE NOISE OF THE EFFECTIVE LOCAL OSCILLATOR WAVEFORM IN HARMONIC REJECTION MIXER,**
   Ludwig Lubich, Technical University of Sofia, Bulgaria

4. **FREQUENCY DOMAIN ANALYSIS OF BIOMEDICAL SIGNALS,**
   Viktor A. Nedialkov, Technical University of Sofia, Bulgaria

5. **MULTIFUNCTIONAL SYSTEM FOR PHYSIOTHERAPY,**
   Atanas Dimitrov, Sasho Guergov, Dimiter Tz. Dimitrov, Technical University of Sofia, Bulgaria

6. **DEVICE FOR ACCUPRESURE WORKING IN MAGNETIC FIELD,**
   Sasho Guergov, Dimiter Dimitrov, Atanas Dimitrov, Technical University of Sofia, Bulgaria

Coffe Break

15h – 15h 30min

CLOSING CONFERENCE SESSIONS

15h 30min– 16h
Building of Library, fourth floor
Technical University of Sofia, Bulgaria

SOCIAL PROGRAM

- **Conference Dinner**, 19h, October 12th
- **Trip**, October, 13th.

  More information regarding Conference dinner and trip will be provided during the first day of the Conference (October 12th)

CONTACT US:

http://oldweb.tu-sofia.bg/eng_new/fktt/cema16

Submission of contributions

Prof. Dr. Dimiter Dimitrov

Faculty of Telecommunication
Technical University of Sofia
8, Kliment Ohridsky str.
1756 Sofia, Bulgaria
Phone:++359 2 9652278
Fax: ++359 2 9652278
E-mail: dcd@tu-sofia.bg

Cultural programme and hotel reservation

Prof. P. Frangos

National Technical University of Athens
School of Electrical and Computer Engineering
9, Iroon Polytechniou Str. ,
157 73 Zografou, Athens, Greece
Phone : 00 30 210 772 3694
Fax : 00 30 210 772 2281
E-mail : pfrangos@central.ntua.gr

TABLE OF CONTENTS

AN APPROACH FOR COLORECTAL POLYP SEGMENTATION

Veska M. Georgieva

Faculty of Telecommunications, Technical University of Sofia, Bulgaria
1000 Sofia, 8 "Kl. Ohridski" blvd.

T. (+359 2) 965-3293; E-mail: vesg@tu-sofia.bg

Plamen P. Petrov

Faculty of Mechanical Engineering, Technical University of Sofia, Bulgaria
1000 Sofia, 8 "Kl. Ohridski" blvd.

T. (+359 2) 965- 3271; E-mail: ppetrov@tu-sofia.bg

Abstract

In this paper, we present an effective approach for colorectal polyp segmentation by processing of endoscopy images.

In regard to quality limitations of colonoscopy images, a preprocessing stage is proposed. It consists of noise reduction with modified homomorphic filter based on wavelet packet decomposition of the transformed image, additionally correction of illumination and contrast enhancement based on CLAHE. The segmentation of colorectal polyps is based on active contour without edges.

Some experimental results are presented, obtained by computer simulation in the MATLAB environment. Implementation results demonstrate the effectiveness of the proposed approach for application in screening diagnostics.

1. INTRODUCTION

Colorectal carcinomas are the most common malignancies in industrialized countries, and can be classified as early or advanced according to the depth of invasion. Early colon carcinoma may occur in an adenomatous polyp and may be difficult to distinguish from a nonmalignant adenomatous polyp by colonoscopy. It is usually revealed by screening colonoscopy and may be curatively treated.

Important risk factors for the polyp malignancy include large size and high numbers of colonic polyps [1]. Based on endoscopic appearances, the advanced colorectal carcinoma can be divided into 4 groups, which are presented on Fig. 1. Type 1 lesion is characterized with protuberant tumor with fold convergence. Type 2 lesions show an irregular ulceration and clear marginal swelling. The lesion of Type 3 shows an irregular ulceration and unclear marginal swelling. The lesion of Type 4 is characterized with irregularly edematous mucosa with luminal stenosis due to diffuse infiltration.

Polyp segmentation is a challenging task. First, the intensity difference between a polyp and colon lumen (air) is apparent, the image intensity is quite similar between the polyp and its surrounding tissue. The low image contrast in a polyp's region makes automated polyp segmentation difficult. Therefore, polyps vary in shape, size, and location. The single shape or densitometry template is not sufficient to characterize all polyps

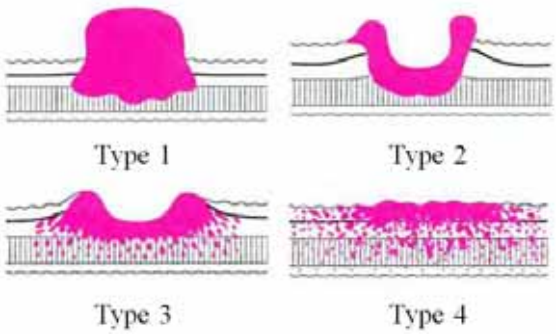

Figure 1. Macroscopic types of advanced colorectal carcinoma [1]

There are number of polyp segmentation methods, which have been reported in the literature [2]. Canny operator and the Radon transform are used to detect polyp boundaries [3]. Using structural entropy a fuzzy decision method for finding polyps is developed [4]. An adaptive deformable model is used to present segmented polyps [5]. Geodesic active contours with a modified speed function on the colon surface are evolved to detect polyp neck regions [6]. By using level-set method the polyp mass region is extracted [7]. Lu et al. propose a classification scheme to segment polyps [8]. Histograms are used to determine the threshold that

would separate polyps from their surrounding tissue [9]. The prior knowledge of polyp shape is used in model-based approach for segmentation [10]. So the accurate measurement of polyp size was obtained because the pose of a polyp is well-defined.

We propose to segment the colorectal polyps via active contour model without edges. In regard to quality limitations of colonoscopy images, a pre-processing stage is proposed.

The paper is arranged as follows: In Section 2 is presented the main algorithm of processing; in Section 3 are given some experimental results, obtainned by computer simulation and their interpretation; in Section 4 - the Conclusion.

2. MAIN ALGORITHM OF PROCESSING

The flowchart of the main algorithm for colonoscopy image processing is given in Fig. 2.

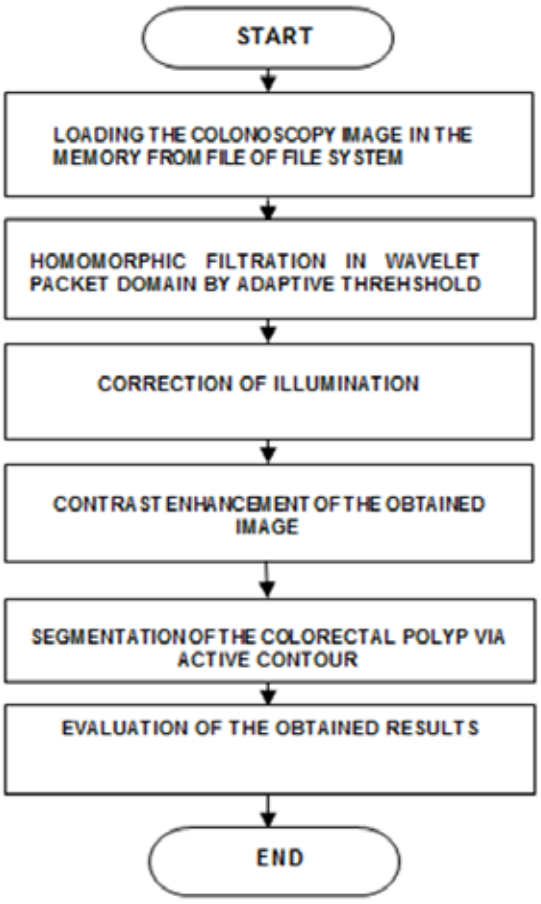

Figure 2. Flowchart of the maim algorithm

The pre-processing stage includes noise reduction with modified homomorphic filter based on wavelet packet decomposition of the transformed image and adaptive threshold of the wavelet coefficients [11]. The modified homomorphic filter uses the illumination-reflectance model in its operation. This model presents the image *f(x,y)* by two primary components. The first component is the amount of source illumination incident on the scene being viewed *i*(*x*,*y*). The second component is the reflectance component of the objects on the scene *r*(*x*,*y*). The intensity of *i*(*x*,*y*) changes slower than *r*(*x*,*y*). Therefore, *i*(*x*,*y*) is considered to have lower frequency components than *r*(*x*,*y*). Using this fact, homomorphic filtering technique aims to reduce the significance of *i*(*x*,*y*) by reducing the low frequency components of the image. This is made by executing the filtration in the frequency domain. However, before the transformation takes place, a logarithm function has been used to change the multiplication operation of *r*(*x*, *y*) with *i*(*x*, *y*) into an addition operation.

The modified homomorphic filtering schema is shown on Fig.2, where WPT is 2D Discrete Wavelet Packet Transformation, H(u,v) presents a filter function, IWPT is 2D Inverse Discrete Wavelet Packet Transformation.

Figure 3. Structure of modified homomorphic filter based on WPT

Because the noise of wavelet transformation usually concentrates on the state of high resolution, the method is useful for successfully reduction of noise in colonoscopy images. The filtration is obtained on the basis of the best shrinkage wavelet packet decomposition and the spatial adapted threshold [11]. The wavelet thresholding procedure removes noise by thresholding only the wavelet coefficients of the detail sub-bands and keeps the low resolution coefficients.

Then additionally, correction of illumination based on background subtraction by morphological processing and contrast enhancement based on CLAHE is applied. The background of the obtained images is estimated by mathematical morphology opening or closing. Then it is subtracted from the original image. The total sequence of operations corresponds to a top hat of the image. We use a disc structuring element greater than the size of the light objects (characters), which are typical for the corresponding colorectal images. The procedures noise reduction and CLAHE are applied to an im-

age, processed in YUV system for more effectiveness.

The colorectal polyp segmentation is made by the implementation of the Chan and Vese active contour model [12]. It is a special case of the Mumford–Shah problem. We consider *f* to be the given grayscale image on a domain Ω to be segmented. Mumford and Shah approximate the image *f* by a piecewise-smooth function *u* as the solution of the minimization problem. Compared to the piecewise constant Mumford - Shah model, the key differences with the Chan - Vese model are an additional term penalizing the enclosed area and a further simplification that *u* is allowed to have only two values, given in (1)

$$u(x)=\begin{cases} c_1 \ where \ \ x \ \ is inside \ \ C \\ c_2 \ \ where \ x \ is \ outside \ C \end{cases} \qquad (1)$$

where *C* is the boundary of a closed set and c_1, c_2 are the values of *u* respectively inside and outside of *C* [13].

By the method of Chan and Vese is proposed to find among all *u* of this form the one that best approximates *f*, which is given in (2).

$$\begin{aligned} u(x) = arg \min_{c_1,c_2,C} \mu Lenght(C) + \\ + \nu Area(inside(C)) + \\ + \lambda_1 \int_{inside(C)} |f(x)-c_1|^2 dx + \\ + \lambda_2 \int_{outside(C)} |f(x)-c_2|^2 dx \end{aligned} \qquad (2)$$

Using the first term we can control the regularity by penalizing the length. The area of *C* and its size can be controlled by second term. The third and fourth terms penalize discrepancy between the piecewise constant model *u* and the input image *f.* By finding a local minimizer of this problem, a segmentation is obtained as the best two-phase piecewise constant approximation *u* of the image *f* [13]. In this case the minimization requires over all set boundaries *C* by using the level set technique introduced by Osher and Sethian [14]. We use a level set function *φ* for a circle of radius *r*. Instead of manipulating *C* explicitly, it is represented as the zero-crossing of a level set function *φ,* given in (3)

$$C = \{x \in \Omega : \varphi(x) = 0\} \qquad (3)$$

The parameters which can be selected for segmentation are following:

- ✓ *mask* – Initial contour as circle, which the evolution of the segmentation begins;
- ✓ *n – Maximum number of iterations* to perform in evolution of the segmentation;
- ✓ *R –Radius of the location in pixels;*
- ✓ *Alpha* – 'Smooth Factor' – Degree of smoothness or regularity of the boundaries of the segmented regions.

The procedure of segmentation begins after choosing all input information. Then the final result from segmentation is visualized – colorectal image with segmented polyp.

3. EXPERIMENTAL RESULTS

The formulated stages of processing are realized by computer simulation in MATLAB 7.14 environment by using IMAGE PROCESSING and WAVELET TOOLBOXES [15]. In analysis are used 30 images with colorectal polyps. It is used database of the colonoscopy images with size 574 x 500 [16], also database from Medical Academy Sofia of colonoscopy images with size 574 x 500 in bmp file format. Some results from simulation, which illustrate the working of proposed algorithm, are presented in the next figures below.

In Fig. 4 is shown the original image with colorectal polyp.

Figure 4. Original colorectal image

Fig. 5 illustrates the pre-processed image.

The graphical presentation of background surface is given in Fig. 6.

The segmented polyp and the grayscale colorectal image with segmented polyp are given on Fig. 7 and Fig. 8 respectively. The segmentation is performing by *n=100* iteration.

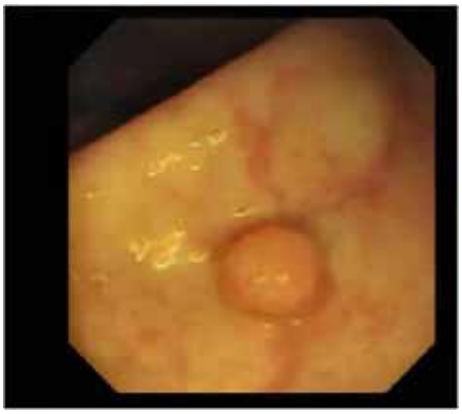

Figure 5. Pre-processed colorectal image

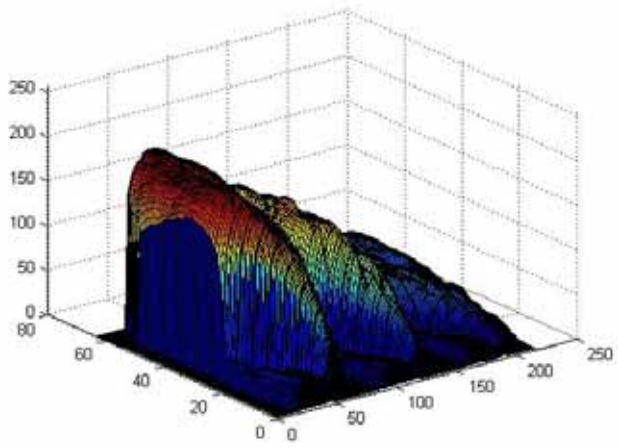

Figure 6. Graphical presentation of background surface

For validation of the segmentation results, we compute the undirected partial Hausdorff distance [17] between the boundary of the computed segmentation and the boundary of the manually-segmented ground truth.

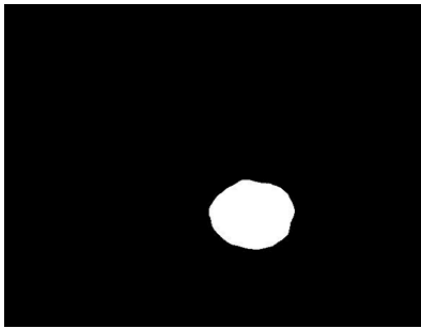

Figure 7. The segmented polyp after 100 iterations

The obtained averaging results for the partial Hausdorff distance between automatic segmentation and the manually-segmented ground truth are given in Table 1.

Figure 8. The grayscale colorectal image with segmented polyp

The obtained averaging results for the partial Hausdorff distance between automatic segmentation and the manually-segmented ground truth are given in Table 1.

Table1. Partial Hausdorff Distance

Method	K [%]
Manually-Segmentation	90.5
Active Contour Segmentation	96

The results shown in Table 1 indicate that virtually all the boundary points lie within some pixels of the manual segmentation, but the segmentation is better in the case of the proposed approach. Higher values of *Alpha* can produce smoother region boundaries but can also smooth out finer details. Lower values produce more irregularities (less smoothing) in the region boundaries but allow finer details to be captured.

4. CONCLUSION

In this paper is presented an effective approach for semi-automatic colorectal polyps segmentation. For enhancement of the colonoscopy images a preprocessing stage is proposed. It consists of noise reduction with modified homomorphic filter based on wavelet packet decomposition. Additionally correction of illumination and contrast enhancement based on CLAHE is made. The method of segmentation is based on active contour without edges. The implemented study and obtained results have shown a high validation of the segmentation. The proposed approach can be applied for screening of early colorectal carcinoma, especially by sigle colorectal polyps.

Our future work will be concentrated in hybrid methods for segmentation and classification of the

polyps in regard to obtain more precise diagnoses. It can be used also in monitoring the disease progression.

5. ACKNOWLEDGMENTS

The paper was supported by the PhD Students Research Project "Algorithms for automatic segmentation of large-scale medical image data", NIS № 162 PD0001-07/2016.

The authors are exceptionally grateful to Professor Dr. V. Hadjidekov at the Department of Image Diagnostic on the Medical Academy in Sofia for the images and advice for the investigations.

References

[1] H. Kashida, SE. Kudo, "Early colorectal cancer: concept, diagnosis and management", Int. J. Clin. Oncol, Vol. 11. No. 1. pp. 1-8, 2006.

[2] V. B. Surya Prasath, "Polyp Detection and Segmentation from Video Capsule Endoscopy: A Review", Journal of Imaging, vol.3, issue 1, pp.1-15, 2017.

[3] A. K. Jerebko, S. Teerlink, M. Franaszek, R. M. Summers, "Polyp segmentation method for CT Colonography computer-aided detection", SPIE Medical Imaging, 5031, pp.359–369, 2003.

[4] S. Nagy, F. Lilic. L. Koszy, "Structural entropy based fuzzy partitioning method for finding polyps on colonoscopy images", IEEE AFRICON 2017, in print.

[5] J. Yao, R.M Summers, "Adaptive deformable model for colonic polyp segmentation and measurement on CT Colonography", Medical physics 34, pp. 1655–1664, 2007.

[6] S. Tan, S., Yao, J., Ward, R. M., Summers, "Linear measurement of polyps in CT Colonography using level sets on 3D surfaces", In: Engineering in Medicine and Biology Society, Annual International Conference of the IEEE, pp. 3617–3620, 2009.

[7] J. J. Näppi, H. Frimmel, A. H. Dachman, H. Yoshida, "Computerized detection of colorectal masses in CT Colonography based on fuzzy merging and wall-thickening analysis", Medical physics 31, pp. 860–872, 2004.

[8] L. Lu, et al., Accurate polyp segmentation for 3D CT Colongraphy using multi-staged probabilistic binary learning and compositional model. In: IEEE Conference on Computer Vision and Pattern Recognition, pp. 1–8, 2008.

[9] S.E Grigorescu, et al.: Automated detection and segmentation of large lesions in CT Colonography. IEEE Transactions on Biomedical Engineering,vol.57, issue 3, pp. 675 – 684, 2010.

[10] Xu Haiyong, H. Donald Gage, Pete Santago, and Yaorong Ge, "Colorectal Polyp Segmentation Based on Geodesic Active Contours with a Shape-Prior Model", Lecture Notes in Computer Science, Virtual Colonoscopy and Abdominal Imaging. Computational Challenges and Clinical Opportunities, pp. 134-140, Springer, 2011.

[11] V. Georgieva, S.Nagy, A. Horvath, E. Kamenova, "An Approach for Pit Pattern Recognition in Colonoscopy Images", Egyptian Computer Science Journal, Vol.39, №2 , pp. 72-82, 2015

[12] T. Chan, L.Vese, "Active Contours Without Edges", IEEE Transactions on Image Processing, vol.10, № 2, pp.266-276, 2001.

[13] P. Getreuer, "Chan-Vese Segmentation", Image Processing On Line, vol.2, pp. 214-224, 2012.

[14] S. Osher, J.A. Sethian,"Fronts propagating with curvature-dependent speed algorithms based on Hamilton-Jacobi formulations," Journal of Computational Physics, vol. 79, no. 1, pp. 12-49,1988.

[15] MATLAB User's Guide. Accessed at: www.mathwork.com

[16] J. Bernal, J.Sánchez, F. Vilariño, "Towards automatic polyp detection with a polyp appearance model", Pattern Recognition, vol. 45, issue 9, pp. 3166–3182, 2012. http://mv.cvc.uab.es/projects/colon-qa/cvccolondb

[17] M.Leventon, W.Grinson, O.Faugeras, "Statistical Shape Influence in Geodesic Active Contours", Computer Vision and Pattern Recognition, vol.1, pp.316-323, 2000.

3D VISUALIZATION OF THE SPLEEN FROM MRI SEQUENCES

Antonia Mihaylova

Faculty of Telecommunications, Technical University of Sofia, Bulgaria
1000 Sofia, "Kl. Ohridsky" str.8

E-mail: antonianankova@gmail.com

Abstract

The modern medical imaging is using more often 3D volume visualization of organs for better observation of the anatomical structure and medical diagnostic. This paper proposes an algorithm for 3D visualization of a segmented human spleen, extracted from a sequence of MRI-images. Such visualization is a logical processing step in a depth comprehensive processing of a sequence of medical images which is preceded of preprocessing and segmentation of anatomical structures.

1. INTRODUCTION

The form of the human spleen is very variable by the different individuals. So the visualization of this organ is very interesting and helpful by studying its shape, functionality and disorders. The spleen has the same relationship to the circulatory system that the lymph nodes have to the lymphatic system [1]. A wide range of diseases can affect the spleen. MR imaging is an excellent tool for diagnosis and evaluation of focal lesions and pathologic conditions of the spleen. Also for studies of health, because of the harmless magnetic field that is used by MRI.

To be visualized the spleen has to be segmented first. There are a lot of segmentation techniques, but not all of them are giving good results in the different cases. Because of the partial volume effect, the gray level of the spleen and grayscale similarity of the adjacent abdominal fat, spleen segmentation has always been a problem [2]. In this case an active contour method for segmentation has been chosen. The "Active Contours Without Edges" by Chan and Vese, that ignores edges completely [3], has been studied in previous work [4, 5] and has shown very good results by the spleen segmentation from abdominal MRI images. After segmenting the spleen from all of the images in a MRI-sequence is used a 3D volume visualisation, that is based on isosurfaces. An Isosurrace can be described as a level set of a continuous function in a 3D-space domain. It is a surface that represents points of a constant value within a volume of space [6]. Before the segmentation and 3D Visualization we can use different filtration and morphological operation if the image data requires it.

2. 3D VISUALIZATION USING ISOSURFACES

An Isosurface can represent Voxels in various types of medical images with Colocalization level. Those points can be joined to form a 3D surface. As all methods and techniques the Isosurface has its own specific calculation method. The 3D dataset is first thresholded at a certain level. The isosurface is the surface that envelops the remaining voxels. The marching cubes algorithm was first published in the 1987 SIGGRAPH proceedings by Lorensen and Cline [6], and it creates a surface by intersecting the edges of a data volume grid with the volume contour. Where the surface intersects the edge the algorithm creates a vertex. The algorithm creates a surface by using table of different triangles, which depends on different patterns of edge intersections. In the modern image processing there are already upgraded Isosurface algorithms such as Scalar Algorithms [8], Surface Nets, Dual Contouring and Isosurfaces and Level-sets [9].

2.1. Scalar field Visualization: Isosurface

Scalars are single data values associated with each point and/or cell of a dataset [10]. Because scalar data is commonly found in real-world application also in MRI images, many different visualization algorithms exists: e.g. Color Mapping, Contouring, Scalar Generation. Color mapping that is used also in the proposed approach in this paper is a common scalar visualization technique. It maps scalar data to colors and displays the colors using standard implemented facilities of the graphic libraries. For this purpose color lookup table is often used. According the table the scalars s_i have minimum and

maximum range into which the scalar values are mapped.

$$\begin{aligned} s_i < min, k = 0 \\ s_i > max, k = n - 1 \\ k = n\frac{s_{i-min}}{max - min} \end{aligned} \quad (1)$$

In the case in this paper the choice of the look up table is not so hard, because we have an already segmented structure that should be in one colour. Other colours are used by representing different sections of the organ to distinguish the outer structure from the inner.

3. ALGORITHM FOR 3D VISUALIZATION OF THE SPLEEN

The algorithm of the approach is presented in the Block diagram, shown in Fig. 1.

The first step is to load a sequence from abdominal MRI – images. In the pre-processing step a Homomorphic-Wavelet Filtration is applied to the images that represent the spleen. The filtration method is chosen, because of the best SNR-results for MRI-images that it showed in a previous study [11].

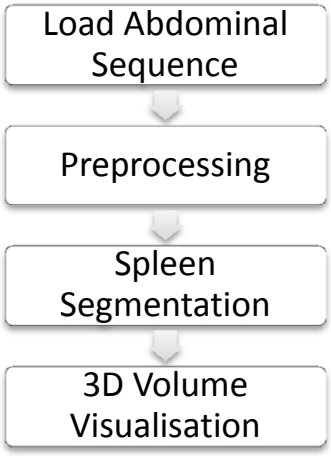

Figure 1. Flowchart of the main algorithm for 3D visualization of the spleen

The filtration is needed for reaching better results in the next segmentation step. The method of active contours without edges combined with level sets is giving the desired accurate binary segments from the MRI-images (Table 1).

Table 1: Experimental quantitative results: average Dice similarity coefficient and Implementation time for each tested method [5]

Segmentation method	Dice similarity difference (%)	Time (s)
Active Contour Without Edges	95.14	22.428
Active Contour With Edges	93.99	23.846
Region Growing	78.65	7.152

Another reason for using it as segmentation method in this approach is that the method is semi-automated and shortens the time for this part of the processing.

The last stage is the Volume Visualization, which includes:

- Building an array from the obtained segmented images;
- Removing singleton dimensions from the array;
- Color mapping the images from the array;
- Drawing the contours of the binary segments in volume slice planes;
- Drawing a patch of extracted isosurface data from volume data;
- Computing normals of isosurface vertices;
- Computing isosurface end-cap geometry;
- Setting face and edge colors;
- Specifying the view;
- Adding lights.

4. EXPERIMENTS AND VISUALIZATION

Many experiments have been conducted for evaluating the effectiveness of the proposed approach. The input image data includes 10 sequences of abdominal MRI-images from a study of health in Pomerania (East Germany). The sequences consist of 64 MRI-images each. They are in DICOM format with size 256 x 176 pixels and are in greyscale. The images from the study are representing no internal diseases or tumors. The volunteers are clinically healthy. The pathological indications were removed from the data base. Other specification of these images is that there quality is not as high as by

regular MRI examinations, because the time for the examination was shorter according to the purposes of the study. The experiments for spleen segmentation are made by computer simulation in MATLAB R2013 environment by using of IMAGE PROCESSING TOOLBOXES. In this paper are presented the obtained results by processing of one of the sequences. In this sequence the spleen were visible in 23 of all of the images (Fig.2).

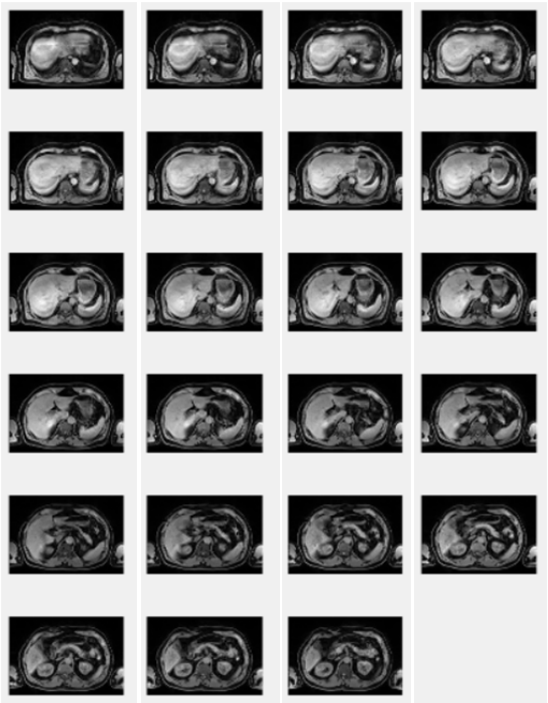

Figure 2. Sequence of 23 original images visualizing the Spleen

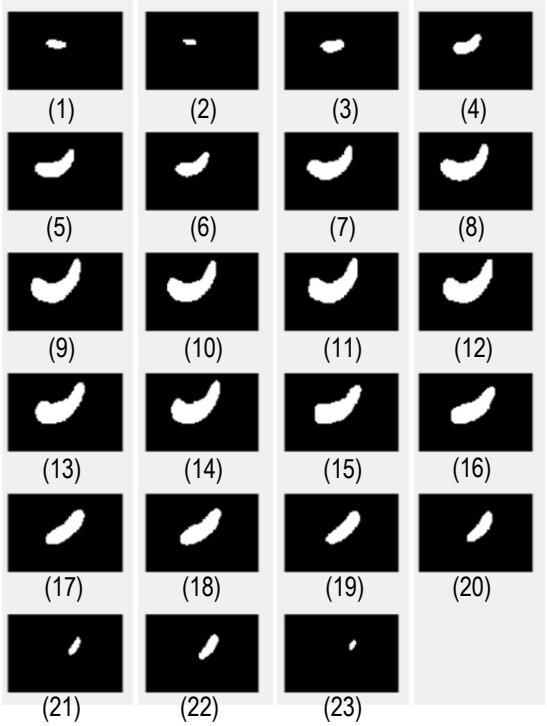

Figure 3. Sequence of the segmented spleen using active contours without edges

The obtained images after segmentation with active contours without edges are shown in Fig. 3. It is used a new method based on active countours that process the images from the sequence automatically. The mean Dice similarity index for the whole sequence is 78.7%. The curve on Fig.4 is representing the variance of the Dice coefficient from the first to the last image in the sequence. The coefficient for the images in the middle of the sequence, where the spleen is bigger, are very high (over 90% for images number: 8 ÷ 18).

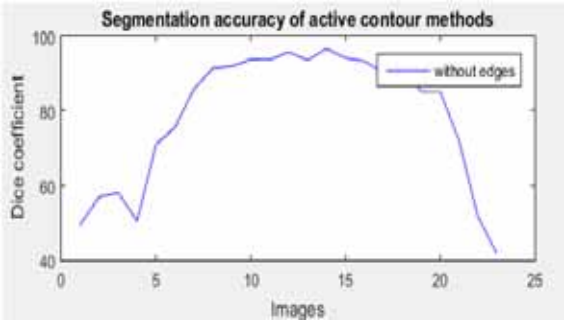

Figure 4. Variance of Dice coefficient for spleen segmentation from sequence of abdominal MRI images

On Fig. 5 are represented different stages from the 3D Volume Visualization method: Color mapping; Drawing contours of one segment; Drawing contours of several segments (layers) in volume slice plane.

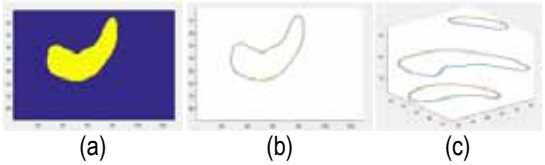

Figure 5. Image (a) is segmented spleen from image number: 9 on Fig.3 with colour map "parula"; (b) represents the contour of the segment and (c) is showing three contours of three different segments from images number: 7, 9 and 19 on Fig.3, but in volume slice plane

The final 3D Volume visualization of the whole spleen is on Fig. 6.

On Fig. 7 is a 3D visualization of the spleen from the same sequence, but segmented manually by hand. Although the relatively high Dice similarity index for the previously used segmentation method, it is obvious in the comparison between the two 3D visualizations that some part of the spleen segmented with the method based on Active contours is missing. So the 3D Visualization method could be very useful by evaluating of the accuracy of segmentation methods applied on image sequences.

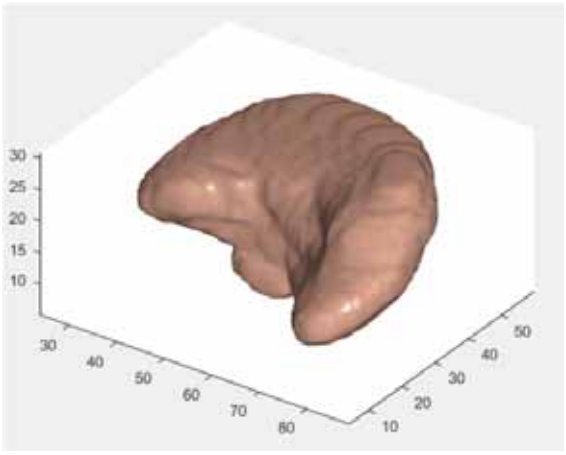

Figure 6. 3D volume visualization of the spleen segmented semi-automatically

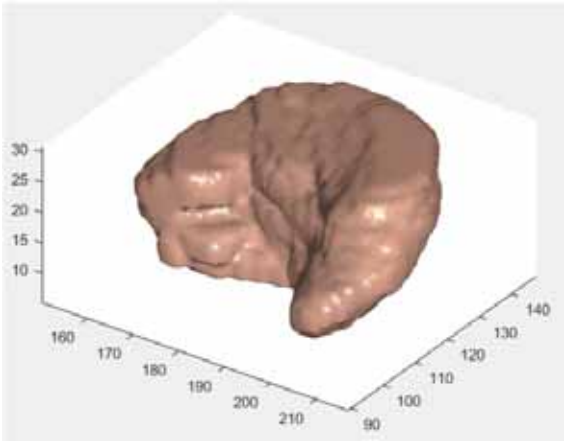

Figure 7. 3D volume visualization of the spleen segmented manually

5. CONCLUSION

The proposed approach for 3D Visualisation of the spleen has shown many applications in the analysis of abdominal MRI images. The conducted experiments enlarged these applications, by showing the capabilities of evaluating the accuracy of different spleen segmentation methods.

6. ACKNOWLEDGMENTS

The paper was supported by the PhD Students Research Project "Algorithms for automatic segmentation of large-scale medical image data", NIS № 162 PD0001-07/2016.

References

[1] Elsayes and All, "MR Imaging of Spleen: Spectrum of abnormalities", RadioGraphics 2005; Volume 25:967–982; Published online 10.1148/rg.254045154.

[2] Alireza Behrad, Hassan Masoumi, "Automatic Spleen Segmentation in MRI Images using a Combined Neural Network and Recursive Watershed Transform", IEEE 10th Symposium on neural network applications in Electrical Engineering, Faculty of Electrical Engineering, University of Belgrade, Serbia, SEPTEMBER 2010

[3] Pascal Getreuer, "Chan and Vese Segmentation" IPOL 2012-08-08 ISSN 2105-1232, Yale University

[4] A. Mihaylova, "Segmentation of Spleen with Pathology from abdominal MRI", Proceedings of 52nd International Scientific Conference on Information, Communication and Energy Systems and Technologies – Serbia, Niš, June 28 – 30, 2017.

[5] A. Mihaylova, V. Georgieva, D. Zlatareva, "Spleen Segmentation in MRI images", Specialized Journal of Radiology and Rentgenology, Number 1, Volume LVI, Jun 2017, ISSN 0486-400X, pp.

[6] William E. Lorensen, Harvey E. Cline: Marching Cubes: A high resolution 3D surface construction algorithm. In: Computer Graphics, Vol. 21, Nr. 4, July 1987

[7] Tao Ju, Frank Losasso, Scott Schaefer, Joe Warren: Dual Contouring of Hermite Data. In: ACM Transactions on Graphics, Volume 21 Issue 3, July 2002

[8] Charles D. Hansen; Chris R. Johnson (2004). Visualization Handbook. Academic Press. pp. 7–11. ISBN 978-0-12-387582-2.

[9] R. Whitaker, "Isosurfaces and Level-Sets", Visualization Handbook. Academic Press. pp. 7–11. ISBN 978-0-12-387582-2. Page 97-122

[10] W. Shroeder and K.Martin, "Overview of Visualisation", Visualization Handbook. Academic Press. pp. 7–11. ISBN 978-0-12-387582-2. Page 3-38

[11] A. Mihaylova, V. Georgieva, "Comparative analysis of Various Filters for Noise Reduction in MRI Abdominal Images", International Journal "Information Technologies & Knowledge" Volume 10, Number 1, © 2016, Page 47-66

[12] Silverstein, Jonathan C.; Parsad, Nigel M.; Tsirline, Victor (2008). "Automatic perceptual color map generation for realistic volume visualization". Journal of Biomedical Informatics. 41 (6): 927–935. ISSN 1532-0464. doi: 10.1016/j.jbi.2008.02.008.

FRACTAL ANALYSIS METHODS IN INVESTIGATION OF ULTRALOW DOSES EFFECTS

Nataly Ampilova, Igor Soloviev

Assoc. Prof. at Comp. Sci. Dept. of St. Petersburg State University
Universitetsky pr. 28, 198504, Starii Peterhof, St. Petersburg, Russia

E-mail: n.ampilova@spbu.ru,
E-mail: i.soloviev@spbu.ru

Abstract

The methods of fractal and multifractal analysis are now widely used because they allow us to analyze and classify digital images with complex structure. We present the results of application of these methods to images obtained by sensitive crystallization method. It was developed for studying blood images and now finds increased use in analysis of medicines, determination of food and soil quality. It seems these methods are rather perspective both in comparing images from different classes and in obtaining a classifying sign for a group of images. Problems arising in images classification are also discussed.

1. INTRODUCTION

Investigation of many natural processes is often based on digital images which show the process states at different instants of time. We consider images of EMF distribution, EEG records, invariant sets of dynamical systems or clusters growing in diffusion process.

As a rule the first analysis of an image we perform visually. Our vision defines differences in image structure by revealing topological invariants – objects that may be considered as image peculiarities. Expert knowledge is based on such a perception: to find an image feature an expert mentally constructs an associative series of images and presents the result of observation as a description of the image structure.

When using mathematical methods of image analysis we also tend to obtain a feature that may be considered as a description of an image structure. Thus our methods are based on formalization of our visual perception – the formalization of expert knowledge. The methods using appropriate formalization that may lead to defining topological invariants seems to be rather promising and give reliable results.

The analysis of images illustrating low doses effects is mainly solved by visual method. By now in this area of research methods of sensitive crystallization and capillary dynamolysis gain wide acceptance. Sensitive crystallization method is based on adding low doses of a matter (blood, plants extract, food) to cuprum chloride solution. By the form of the obtainned crystal one may decide on an organism (for blood crystals) or the added matter state. Capillary dynamolysis method is application of a solution of a matter (made by a definite method) to filtering paper.

Sensitive crystallization now may be successfully applied in the analysis of food, homeopathic preparations [3, 7, 12], and capillary dynamolysis is widely used in the analysis of soil [8]. The images obtained by the mentioned methods have extremely rich and complex structure, but the experience in application of mathematical methods of analysis is mainly concerned with the second order statistics [3].

Our experience in analyzing biomedical preparation images (in [6] we calculated Rényi spectra for images of pharmacological solutions of Ag) testifies that the good separation of spectra results in successful classification of similar images. In this work we apply fractal signature and multifractal methods to analyze crystals of blood. The results of experiments show that this method is reasonably perspective and may lead to obtaining a set of classifying signs. Moreover, the interpretation of these signs may help in understanding of the intrinsic processes generating such crystals.

2. SENSITIVE CRYSTALLIZATION METHOD

The method of sensitive crystallization was developed by Pfeiffer as early as in 1930h [11], but still is pioneer one. The method is based on addition of

whole blood (or plant extracts) to a solution of cuprum chlorides. The foundations of the method and a systematics of experiments with blood crystals are described in detail in [13]. In [14] the author studied influence of metals on human being and assumed that results of the crystallization may be indirect proof of malfunction of metallic processes in a patient blood. The method also results in defining organs malfunctions and pathological processes in organism. For blood the crystallization by cuprum chlorides is a sensitive morphological test. Pfeiffer considered such a crystal as a picture of the state of the whole organism and connected parts of the body with areas of the test image. The studying of extensive experimental materials resulted in revelation and classification of specific forms in crystallization images, being every class may be matched to a type of disease and the location of a form on the test image corresponds to location of an organ.

It seems the blood formulation (low doses of some substances) defines the type of crystal. Currently the method has attracted considerable interest of many scientists. B. Waldburger [16] assumes that crystal structures demonstrate a dynamic of processes in human organism and discusses perspectives of blood crystal analysis.

The application of rigorous mathematical methods to various kinds of blood crystal images allows us to extract many features such as regular areas, cavities and structures, and find informative classification signs.

3. IMAGE ANALYSIS METHODS

3.1. Multifractal spectrum calculation

Multifractal spectrum of a digital image is a set of fractal dimensions of its fractal subsets. We consider a special density function [17] to calculate the singularity power for every pixel. Then we combine all the pixels with close values of density function, which results in partition of the image on the subsets – so called level sets. For each level set we calculate its fractal dimension.

Let μ be a measure defined through pixel intensities. For $x \in R^2$ we denote $B(x,r)$ a square of length r with center x. Let $\mu\big(B(x,r)\big) = kr^{d(x)}(x)$, where $d(x)$ is the local density function of x and k some constant. Then

$$d(x) = \lim_{r\to 0} \frac{\log \mu(B(x,r))}{\log r}$$

The density function measures the non-uniformity of the intensity distribution in the square $B(x,r)$. The set of all points x with local density α is a level set $E_\alpha = \{x \in R^2 : d(x) = \alpha\}$. In practice, not to increase the number of level sets, one really consider the sets $E(\alpha,\varepsilon) = \{x \in R^2 : d(x) \in [\alpha, \alpha+\varepsilon]\}$.

Then we calculate fractal dimensions of level sets E_α and obtain the multifractal spectrum $f(\alpha)$.

3.2. Fractal signature method

The described method may be applied to calculate (approximately) the area of gray level surface for an image. The technique was described in [4], used for solving various application problems in [10, 9, 5]. We applied this method in different variants to analyze biomedical preparation images [1, 2].

Let $F = \{X_{ij}, i = 0,1,\dots,K, j = 0,1,\dots,L\}$ be a gray level image and X_{ij} be the intensity of the (i,j)-th pixel. In a certain measure range the surface of the function F can be viewed as a fractal. In image processing the function F is a nonempty bounded set in R^3. The surface area A_δ may be calculated using the volume of a special δ-parallel body ("blanket") with the thickness 2δ.

For $\delta = 1, 2, \dots$ the blanket surfaces are defined iteratively as follows:

$$u_\delta(i,j) = \max\left\{ \begin{matrix} u_{\delta-1}(i,j) + 1, \\ \max\limits_{|(m,n)-(i,j)|\le 1} u_{\delta-1}(m,n) \end{matrix} \right\},$$

$$b_\delta(i,j) = \min\left\{ \begin{matrix} b_{\delta-1}(i,j) - 1, \\ \min\limits_{|(m,n)-(i,j)|\le 1} b_{\delta-1}(m,n) \end{matrix} \right\}.$$

The volume of the blanket Vol_δ is

$$Vol_\delta = \sum (u_\delta(i,j) - b_\delta(i,j)).$$

The formulas for the surface area are: $A_\delta = \frac{Vol_\delta}{2\delta}$ or $A_\delta = \frac{Vol_\delta - Vol_{\delta-1}}{2}$. Basing on these formulas one may calculate fractal dimension of the surface, vector of fractal signatures that is the set of values $\frac{\log A_\delta}{\log \delta}$ or divide the area on cells and calculate the dependence of surface area on the size of a partition cell. For color images all experiments are performed in different components of a palette and the component choice may influence on the result considerably.

4. EXPERIMENTS

Experiments were performed for typical images of blood crystals and images obtained by magnification of a part of image.

4.1. Typical forms of blood crystals

The images of crystals correspon-ding some organ malfunctions [15] are shown on Figure 1.

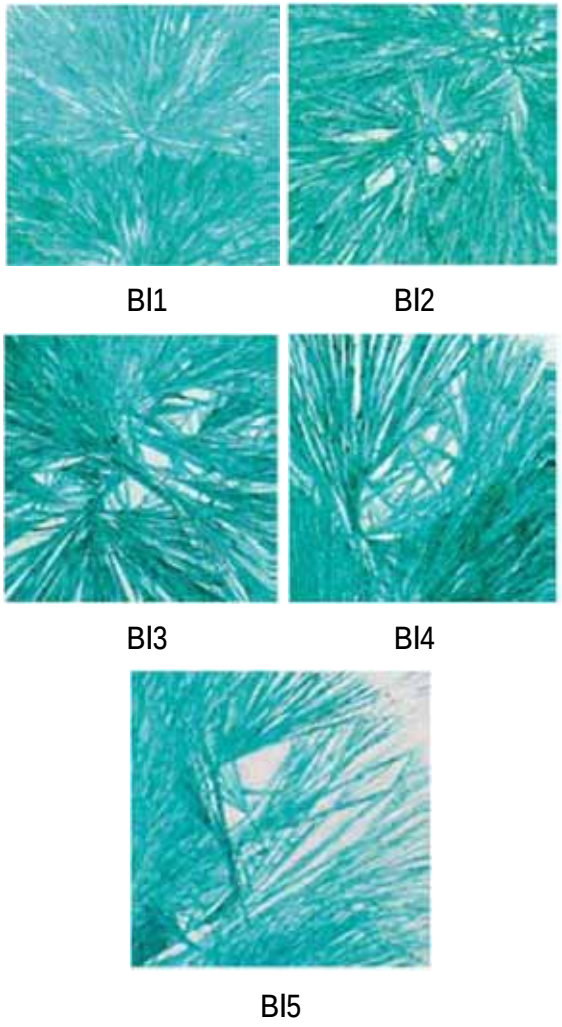

Figure 1. Typical forms of blood crysrtalls

Here Bl1 – crystallization in the star form with hole structure, typical for acute inflammatory process; Bl2 – crystallization in the star form with hole structure, chronic inflammatory process; Bl3 – hole structure of crystals, degenerative processes; Bl4 – hollow form of the crystal, benign tumor; Bl5 – hollow form of the crystal with transversal structures, malignant tumor.

4.1.1. Fractal signature method

The calculation of the dependence of surface area on cell size leads to the following results.

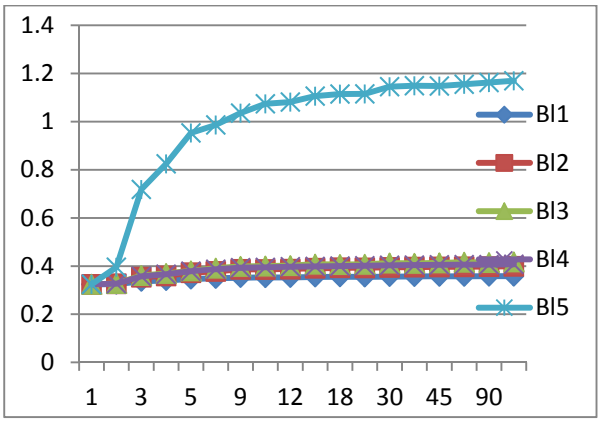

Figure 2. The graphic for malignant tumor is considerably differ from others

4.1.2. Multifractal spectra

On the following graphics singularity values α are on X-axis, and fractal dimensions $f(\alpha)$ — on Y-axis.

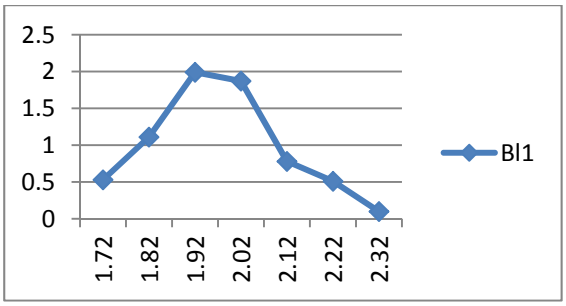

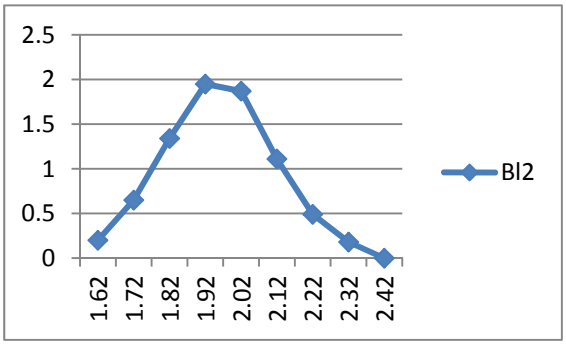

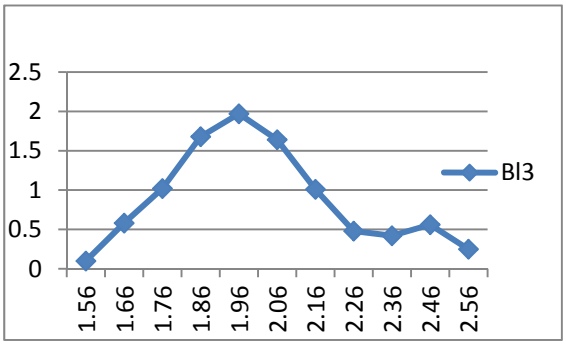

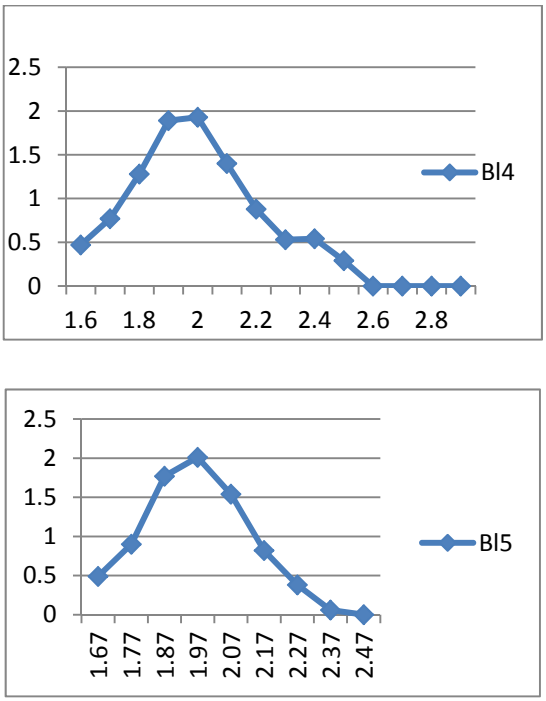

Figure 3. Multifractal spectra calculated by density function

4.2. Magnified images

4.2.1. Fractal signature method

Now we compare the images of blood crystal and carrot crystal.

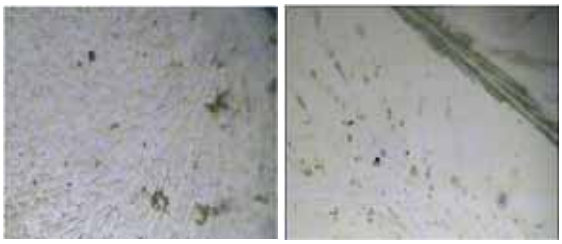

Figure 4. Magnified parts of crystals, blood (left) and carrot (right)

For both images we calculated the dependence the surface area on cell size. The corresponding graphics are shown on Fig. 5.

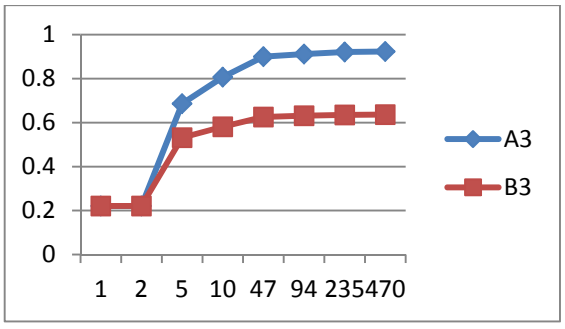

Figure 5. Application fractal signature method to magnified images

4.2.2. Multifractal spectra

Now we consider magnified parts of blood crystal images (parts were taken at the same places) for 3 patients.

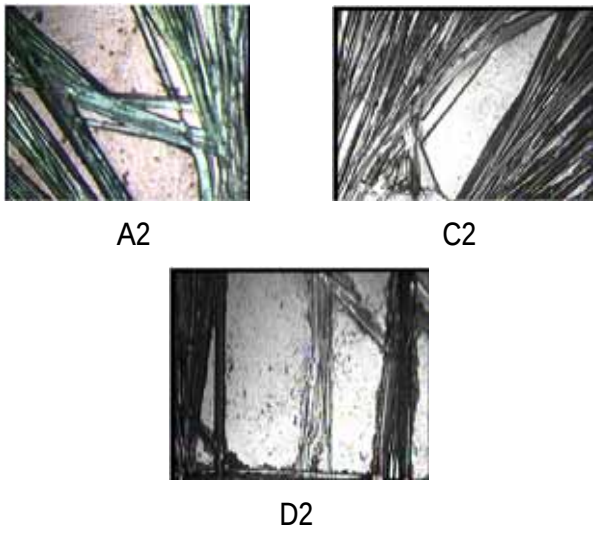

Figure 6. Images obtained by magnification of parts of initial crystals

The results of multifractal spectra calculations are shown below.

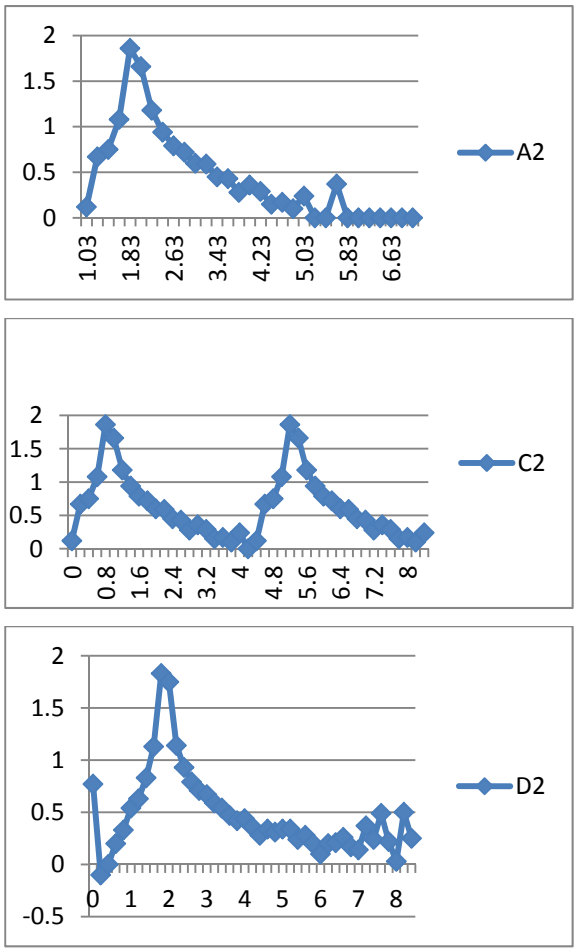

Figure 7. Calculation of multifractal spectra

5. CONCLUSION

The use of multifractal methods to images obtained by sensitive crystallization seems to be very perspective. One may compare images from different classes or find a common sign for a group.

It should be noted that the context is important, because images obtained in different experiments may have similar structures. Hence the classification problem should be solved in collaboration with researchers, and the image structure may be not unique feature to take into account.

6. ACKNOWLEDGEMENTS

Authors wish to express their thanks to V. V. Mujumdar, Managing Director Partner of Institute of Applied Research (IAR), J297, M.I.D.C, Bhosari, Pune, (INDIA) for blood crystallization images.

We also thank E. Kulikov for help in numerical experiments.

References

[1] N. Ampilova, I. Soloviev, "Application of Fractal and Multifractal Analysis Algorithms to Image Segmentation and Classification", WSEAS Transactions on Biology and Biomedicine, ISSN / E-ISSN: 1109-9518 / E-ISSN: 2224-2902, Volume 13, 2016, Art. #3, pp. 14-21.

[2] N. Ampilova, I. Soloviev, Y. Shupletzov. "On some aspects of the fractal signature method", Proc. 8 Int. Conf. CEMA13, 17-19 Oct. 2013, Sofia, Bulgaria, pp. 80-84.

[3] S. Baumgartner, P. Doesburg, C. Scherr, and J.-O. Andersen, "Development of a Bio-crystallisation Assay for Examining Effects of Homeopathic Preparations Using Cress Seedlings", Evidence-Based Complementary and Alternative Medicine Volume 2012, Article ID 125945, pp. 1-14.

[4] K. J. Falconer Fractal Geometry. Mathe-matical Foundations and Applications, John Wiley & Sons, 1990.

[5] P. Frangos, C. Pandis, A. Malamou, P. Stefaneas, "Applying the modified fractal signature method to image classification: some preliminary results for ISAR radar images", Proc. 7 Int. Conf. CEMA12, 8-10 Nov. 2012, Athens, Greece, pp. 50-52.

[6] E. Gurevich, N. Ampilova, I. Soloviev. "On a natural-science investigation of the ultralow doses effect", Proc. 8 Int. Conf. CEMA13, 17-19 Oct. 2013, Sofia, Bulgaria. pp. 85-88.

[7] Kokornaczyk MO, Trebbi G, Dinelli G, Marotti I, Bregola V, Nanni D, Borghini F, Betti L. "Droplet evaporation method as a new potential approach for highlighting the effectiveness of ultrahigh dilutions", Complementary Therapies in Medicine 2014, vol.22, pp. 333—340.

[8] M. O. Kokornaczyk, F. Primavera, R. Luneia, S. Baumgartner & L. Betti, "Analysis of soils by means of Pfeiffer's circular chromatography test and comparison to chemical analysis results", Biological Agriculture & Horticulture, 2016. pp. 1-15.

[9] Xiaogang Mao, C. Y. Suen, "Modified Fractal Signature (MFS): A New Approach to Document Analysis for Automatic Knowledge Acquisition", IEEE Trans. Knowledge and Data Eng., vol.9. no.5, 1997, pp. 742-762.

[10] S. Peleg, J. Naor, R. Hartley, D. Avnir, "Multiple Resolution Texture Analysis and Classification", IEEE Transactions on Pattern Analysis and Machine Intelligence, vol. Pami-6, no. 4, July 1984, pp. 518-523.

[11] E. Pfeiffer. Empfindliche Kristallisation-vor-gange als Nachweis von Formkraften im Blut, Dresden, 1935.

[12] G. Reiter, J.-G. Barth, "Some general re-marks on crystallisation in the presence of additives", Elemente d. N. 92, 2010, pp. 30–61.

[13] A. Selawry, O. Selawry, Kupferchlorid Kri-stallisation im Natiswissenschaft und Medizin. Gustav-Fisher Verlag, Stuttgart, 1957.

[14] A. Selawry, Functional types of metals in Psychology and Medicine, v.2., SPb, Demetra, (in Russian), 2011.

[15] B. Waldburger, Die Empfindliche Kristalli-sation. Eine Methode zur Qualitatatsforschung. Goetheanum Research Institute, The Laboratory for Sensitive Crystallisation, Dornach, 2007.

[16] B. Waldburger, "Die Blutkristallization als Schulungsmethode, Originalia", Der Merkurstas, Heft 5, 2013, p. 402-414.

[17] Yong Xu, Hui Ji, Cornelia Fermuller, "Viewpoint Invariant Texture Description Using Fractal Analysis", Int. J. Comp. Vis, 2009, 83, pp. 85-100.

USER ACTIVITY RECOGNITION IN AUTOMATED CONTROL OF SMART ENVIRONMENT

Artem Kirienko

Comp. Sci. Department, SPbSU
Saint-Petersburg, Botanicheskaya st. 70, b. 4, r.717

E-mail: artem.kirienko@gmail.com

Abstract

The main approach to the activity pattern recognition problem is based on the data obtained from many simple sensors having binary output (e.g. motion sensor, door opening sensor, etc.). We propose a method using Bluetooth beacons RSSI and heart rate sensor data as an input dataset. Basing on the dataset analysis we implemented a simple activity pattern recognition model and evaluated accuracy metrics. The results of experiments show that the method may be successfully used for solving the activity pattern recognition problem. Disadvantages of the simple model and ways to improve it are discussed.

1. INTRODUCTION

There are several approaches to analyze user activity in context of smart environment. The easiest and prevailing approach nowadays is manual set up triggers on particular sensors data, e.g., "turn on the light when motion detected by the sensor". Although this approach is rather simple, it has a set of disadvantages. It requires to set up the system manually by entering all desired triggers. It is not adaptive. Therefore, triggers should be updated manually when user behavior changes. And, the last but not least, it requires many sensors with simple output (such as motion or door opening ones).

Another set of approaches is based on machine learning. One of the first researches related to using machine learning for user activity recognition was performed in MIT research [3], where many simple two state sensors were used as a data source. The sensors were located on different objects that user interacts with (e.g. faucets, doors, oven). The sensors were activated when user interacted with some part of an environment (e.g. opened a door). The disadvantages of this approach are the large number of sensors and the lack of knowledge about user state. Authors had less data sources to choose from than available nowadays. Another relevant research is CASAS project [5]. It utilizes a significant amount of motion sensors located uniformly across an environment. The result is an approximate knowledge about user state (user movements in space). Researches prove that it is a reasonable idea to use data related to user motion in space. However, motion sensors provide only binary data (motion detected / no motion). Such kind of information is barely worth investments into significant number of sensors.

In this work we discuss a possibility to use raw Bluetooth-beacons RSSI data for recognizing user activity in smart environment. This problem is actual in the context of automated control of smart environment. User activity patterns are usually correlated with a desired environment state at the moment when a particular pattern occurs.

The correlation between raw RSSI data and environment state itself was proved earlier [2].

MIT approach has significant disadvantage in the context of automated control problem. It uses environment changes to recognize user activity, but when solving the automated control problem we should control the environment state itself, without direct user interaction. So, some kind of data describing user activity directly, without environment, is required. Actually, in most cases the data describing a user movement in space is appropriate. Such kind of data was collected and researched in CASAS project [5]. Motion sensors spaced one meter apart were used. Later P. Rashidi in his research [6] presented an approach to user activity recognition based on CASAS data.

Although motion sensors describe user movements in space they have only two states. Thus, such sensors provide very limited information about user movement. For example one cannot differentiate if a user is sitting on a sofa or dressing

up close to it. It is preferable to have more information about the user movement and current state.

This kind of information can be obtained by using GPS-navigation idea in local scale. GPS technology measures a satellites signal strength to calculate the position. Local beacons with static position can be used with the same motivation. Then local beacons signal strength can be used to get an information about user position and movement. Nowadays Bluetooth and Wi-Fi modules are widely used in many different devices. These devices can be used as beacons if they have a static position. Also, special beacons can be used, e.g. ones based on iBeacon technology. Such beacons are relatively simple and cheap devices. Five iBeacon-based beacons and two Bluetooth-devices with static position were used for this work.

Unfortunately, the precision obtained by such an approach is barely enough for purposes of user activity recognition (as it was mentioned, for example, in [7]). The main purpose of similar researches was to translate raw beacons RSSI data into Cartesian coordinates. In the context of automated control of smart environment such translation is not required. Moreover, it is the translation that is the main source of precision loss. Without the translation, we were able to obtain data with precision enough even to differ if user is sitting or standing at the same position.

In this work we propose a method to collect more data using less sensors, namely to use Bluetooth beacons instead of motion sensors and analyze RSSI values. In our previous work [2] we considered the using RSSI values to solve automated control problem directly. In this article we apply this method to recognize activity patterns. As activity patterns are directly related to user location, the new approach gives better results as it involves only user state analysis (without an environment state).

2. MODEL DESCRIPTION

The activity recognition problem is a problem of classification where classes are considered as activity patterns. A set of features may vary, but it always should describe an individual behavior inside an environment (directly or indirectly).

There are two general approaches to activity recognition problem: one defines a finite set of activity patterns and marks a dataset according to the patterns set, the second — extracts a set of activity patterns directly from the dataset (using clustering or another similar approach). We start from the first one.

Consider the following set of activity patterns:

- breakfast;
- cooking breakfast;
- cooking dinner;
- dinner;
- entered home;
- leaving home;
- preparing to sleep;
- shower;
- using toilet;
- washing hands;
- watching TV.

We implemented an iOS application to collect dataset and mark it with these activity patterns. The features are Bluetooth beacons RSSI values and heart rate value. They are also collected by the iOS application.

As a result, we have a raw data to analyze in the following format:

- timestamp
- data source UUID
- value
- human readable description

Example (for a beacon):

- 1466771448.85298
- EBEFD083-70A2-47C8-9837-E7B5634DF524
- -79
- HallBeacon

Activity patterns are marked by the same way:

- 517783557.614923
- 7c5d5f96-4667-4d35-9bf1-4cf604e2bc35
- 1
- Watching TV

The value encodes activity start (1) and activity end (0).

The user marks activity patterns manually using the application.

Our task is to construct a model able to classify an activity pattern using the feature set described above as an input data. The usual approach to this problem widely used in other researches ([3][5][8])

is to train a classifier for each activity pattern. In earlier researches the best performance in related problems was provided by SVM. We also start experiments with it.

3. DATA COLLECTION AND EXPERIMENTS

The data collection process was described in detail in our previous work [2]. Only the most important aspects will be described below.

We implemented an iOS application that collects necessary data: Bluetooth beacons RSSI, heart rate sensor data from Apple Watch – and provides a user interface to mark activity patterns. The result is a CSV document with separate row for each event in the following format:

timestamp, UUID, value, description

Possible event types are:

- new data from heart rate sensor;
- new measured RSSI value for a particular beacon;
- activity pattern begin/end.

The user lived in one bedroom apartment. Seven Bluetooth beacons were located uniformly across the apartment (see Figure 1 for the apartment scheme and beacons location). The data were collected for two weeks.

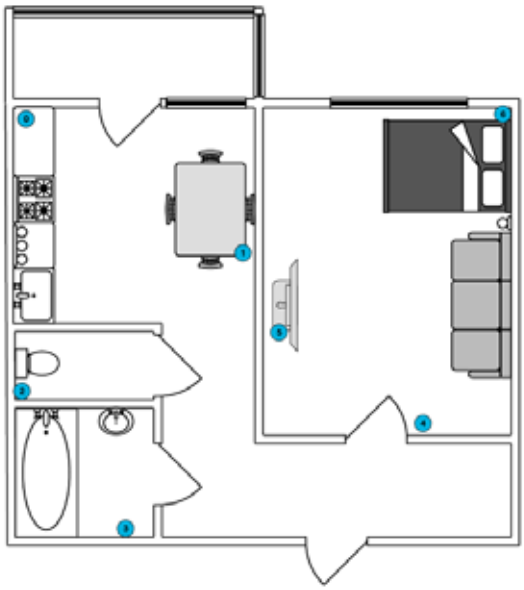

Figure 1. Bluetooth beacons location

4. DATA ANALYSIS

Raw dataset consists of separate records for each event (such as new data from sensor or changes in current activity pattern). To proceed with analysis the dataset should be converted into feature vectors and target values for each particular activity pattern (1 if pattern occurred, –1 if feature vector is not related to the considered pattern).

The feature vectors have the following format:

99, –48, –65, –81, –83, 0, –83, 0

where the first value is a heart rate value and other values are RSSI of beacons (0 corresponds to the beacons that are too far away to measure RSSI).

Consider a subset of data obtained for "Watching TV" pattern (the beginning of observation):

92,-58,-78,0,0,0,0,0,-1

92,-62,-70,0,0,0,0,0,-1

92,-62,-70,0,0,0,0,0,-1

92,-57,-70,0,0,0,0,0,-1

92,-56,-70,0,0,0,0,0,-1

92,-56,-70,0,0,0,0,0,-1

92,-60,-75,0,0,0,0,0,1

92,-60,-75,0,0,0,0,0,1

92,-60,-75,0,0,0,0,0,1

92,-60,-75,0,0,0,0,0,1

Columns 2 and 3 correspond to the beacons #4 and #5 on the Figure 1. Notice that the signal from these beacons become weaker while user is approaching to the sofa.

"Watching TV" pattern in the process of activity:

78,-64,-75,0,0,-83,0,0,1

78,-64,-75,0,0,-83,0,0,1

78,-64,-75,0,0,-83,0,0,1

78,-64,-75,0,0,-83,0,0,1

78,-65,-75,0,0,-82,0,0,1

78,-65,-75,0,0,-82,0,0,1

78,-65,-75,0,0,-82,0,0,1

78,-65,-75,0,0,-82,0,0,1

Notice that the heart rate becomes lower while user is sitting. Another beacon appeared (column 6, beacon #6 on the Figure 1).

"Watching TV" pattern in the end of activity:

78,-62,-74,0,0,-83,0,0,1

78,-69,-74,0,0,-83,0,0,1

78,-69,-74,0,0,-83,0,0,1

78,-60,-76,0,0,-85,0,0,1

78,-60,-76,0,0,-85,0,0,1

78,-60,-76,0,0,-85,0,0,1

78,-60,-76,0,0,-85,0,0,1

78,-65,-77,0,0,0,0,0,1

78,-65,-77,0,0,0,0,0,1

78,-65,-77,0,0,0,0,0,1

78,-54,-77,0,0,0,0,0,1

78,-65,-88,0,0,0,0,0,1

78,-65,-88,0,0,0,0,0,1

78,-65,-88,0,0,0,0,0,1

78,-65,-88,0,0,0,0,0,1

78,-62,-88,0,0,0,0,0,-1

78,-62,-88,0,0,-82,0,0,-1

78,-62,-88,0,0,-82,0,0,-1

78,-62,-88,0,0,-82,0,0,-1

78,-62,-88,0,0,-82,0,0,-1

78,-56,-59,0,0,-82,0,0,-1

78,-56,-59,0,0,-82,0,0,-1

78,-56,-59,0,0,-82,0,0,-1

78,-56,-59,0,0,-82,0,0,-1

78,-56,-59,0,-80,-82,0,0,-1

78,-56,-61,0,-80,-82,0,0,-1

78,-56,-61,0,-80,0,0,0,-1

78,-56,-61,0,-80,0,0,0,-1

78,-56,-61,0,-80,0,0,0,-1

Signal from the beacons #4 and #5 becomes stronger, another beacon appears while user is approaching to the corridor (column 5).

With a little delay, heart rate value is updated:

78,-64,-72,0,-82,0,0,0,-1

78,-64,-72,0,-78,0,0,0,-1

117,-63,-71,0,-78,0,0,0,-1

117,-64,-71,0,-78,0,0,0,-1

The user is moving fast so the heart rate increases.

"Watching TV" pattern is not the most trivial because user is moving around this room a lot and "Watching TV" requires heart rate analysis to recognize that user not just near the sofa, but is sitting on it. It is also a frequently appearing pattern so there is a lot of data to analyze. Other patterns considered have the same or lower recognition complexity.

As a result of preliminary data analysis, we came to conclusion that the data considered definitely correlates to user activity and can be used in activity pattern recognition problem.

5. IMPLEMENTATION

Consider the activity pattern recognition problem in terms of particular choice of input data and corresponding hardware. The dataset consists of beacons RSSI at particular timeframes, heart rate value at every timeframe and manually marked activity patterns occurred while collecting the data.

Taking into account results achieved in related works, radial basis function was chosen as a kernel for SVM. In was the best performer in similar problems. Moreover, our task is to recognize a subspace in RSSI values coordinate space. SVM with RBF kernel was designed to perform this task the best way using an optimal hyperplane principle.

Both classification and data preprocessing were performed using Python programming language as it has many utilities and libraries available that are able to speed up the research process.

Dataset was preprocessed and a classifier was trained for each activity pattern. Cross-validation approach was used with different train and test set distributions (1:2, 1:1, 2:1).

The dataset consists of 164770 samples that were collected for two weeks.

6. RESULTS AND DISCUSSION

Two metrics were used to evaluate the classification quality: accuracy and AUC (area under ROC curve). Accuracy in this case means the time interval when a pattern was recognized right.

Accuracy values for each activity pattern are given in the Table 1.

Table 1. Accuracy evaluated for different activity patterns

Activity pattern	Accuracy (for different test and train sets distribution)		
Breakfast	0.965	0.965	0.965
Cooking breakfast	0.947	0.947	0.947
Cooking dinner	0.962	0.962	0.962
Dinner	0.979	0.979	0.979
Entered home	0.981	0.981	0.981
Leaving home	0.973	0.973	0.973
Preparing to sleep	0.977	0.974	0.969
Shower	0.990	0.990	0.990
Toilet	0.881	0.913	0.892
Washing hands	0.923	0.923	0.923
Watching TV	0.871	0.821	0.887

High accuracy is not determinative without AUC. In this case a particular pattern does not occur as significant portion of time. AUC values for each activity pattern with different train and test set distribution are presented in the Table 2.

Table 2. AUC evaluated for different activity patterns

Activity pattern	AUC (area under ROC curve)		
Breakfast	0.348	0.548	0.561
Cooking breakfast	0.695	0.589	0.601
Cooking dinner	0.703	0.606	0.594
Dinner	0.682	0.518	0.418
Entered home	0.529	0.534	0.552
Leaving home	0.636	0.602	0.590
Preparing to sleep	0.887	0.869	0.870
Shower	0.881	0.949	0.876
Toilet	0.789	0.833	0.812
Washing hands	0.818	0.785	0.768
Watching TV	0.683	0.643	0.622

AUC values are much better than for random guess (which is 0.5). For particular patterns AUC is greater than 0.8. Taking into account the fact that no data filtering was implemented, such result means that the data type considered (beacons RSSI and heart rate) can be used to solve an activity pattern recognition problem even without any additional data sources.

7. CONCLUSIONS AND FUTURE WORK

By analyzing the results we noticed the following:

- data filtering is important for RSSI data (signal can be lost for a couple of timeframes and then appear again);
- manual activity patterns marking is not necessary for the production system (it is still required for research to measure results), clusterization approach can be used to extract activity patterns set.

A dataset containing beacons RSSI values, heart rate data and activity patterns marks was collected and analyzed.

A basic solution of activity pattern recognition problem based on the data sources considered was implemented. The accuracy is from 82% to 99% for different activity patterns. AUC is up to 0.95. The metrics values mean that the data type considered can be used to solve an activity pattern recognition problem without any additional data sources.

The main result is a fact that Bluetooth beacons and an optical heart rate sensor can be used to provide all necessary data to solve an activity pattern recognition problem, at least for particular finite set of activity patterns.

This information can be used to implement further, more complex and accurate solutions.

References

[1] Kirienko A.S., Soloviev I.P. Different approaches to use machine learning in adaptive control of smart environment // Modern technologies in theory and practice of programming, 2016.

[2] Kirienko A.S., Soloviev I.P. Human behavior analysis in context of smart environment automation // Computer tools in education, 2017. № 1. P. 15-29.

[3] Munguia Tapia E. Activity recognition in the home setting using simple and ubiquitous sensors : Ph.D. thesis. – Massachusetts Institute of Technology, 2003.

[4] Choi S., Kim E., Oh S. Human behavior prediction for smart homes using deep learning //RO-MAN, 2013 IEEE. – IEEE, 2013, C. 173-179.

[5] Cook D. et al. Collecting and disseminating smart home sensor data in the CASAS project //Proceedings of the CHI Workshop on Developing Shared Home Behavior Datasets to Advance HCI and Ubiquitous Computing Research. – 2009. – C. 1-7.

[6] Rashidi P. et al. Discovering activities to recognize and track in a smart environment //IEEE transactions on knowledge and data engineering. – 2011. – Т. 23. – №. 4. – С. 527-539.

[7] Oksar I. A Bluetooth signal strength based indoor localization method //Systems, Signals and Image Processing (IWSSIP), 2014 International Conference on. – IEEE, 2014. – С. 251-254.

[8] Stenudd S. Using machine learning in the adaptive control of a smart environment //Utigivare, Vuorimiehentie. – 2010.

PREPROCESSING AND CLUSTERING RAW ACCELEROMETER DATA FROM SMARTPHONES FOR HUMAN ACTIVITY RECOGNITION

Pavel Dinev, Ivo R. Draganov, Ognian L. Boumbarov

Radiocommunications and Videotechnologies Dept.
Faculty of Telecommunications, Technical University of Sofia
8 Kliment Ohridski Blvd., 1756 Sofia, Bulgaria

e-mail: pr_dinev@abv.bg, idraganov@tu-sofia.bg, olb@tu-sofia.bg

Darko Brodić

University of Belgrade, Technical Faculty in Bor, Vojske Jugoslavije 12, 19210 Bor, Serbia

e-mail: dbrodic@tf.bor.ac.rs

Abstract

In this paper is proposed an algorithm for preprocessing and clustering of raw data obtained by accelerometer sensor embedded into a smartphone. It is used by ordinary users while performing sitting, walking and running activities. The goal of the implementation is to enhance the representation of initially generated vectors into compact clusters. As the experimental results reveal it is necessary to introduce an advanced classification approach, such as SVM, in order to recognize the current activity. The method seems promising for application towards users with various medical conditions under remote and prolonged monitoring.

1. INTRODUCTION

Human activity recognition (HAR) becomes increasingly important area of moderm machine intelligence [1, 7, 8]. It includes the ability of automated systems to discriminate various actions performed by humans, such as running, walking, jumping, standing, etc. In the same time the subject is wearing or carrying diferent types of sensors, most often accelerometers. In the recent years buil-in smartphone sensors appeared to be extrmely popular with their low-price and universality wihtin these multipurpose devices [2]. The possible applications include observation of patients with various disabilities in home environment without the presence of medical personnel, monitoring and analysis of actively sporting professionals, investigating the activity performance of military personnel and others [3].

There various methods employed for the recognition of different human activities. In [2-4] Ronao and Cho introduce deep learning neural networks, followed by two-stage continous hidden Markov models, and deep convolutional neural networks. They achieved recognition accuracy up to 95.75%, 96.58% and 99.53% respectively for particular activities.

Committee AdaBoost combining decision trees is proposed by Ugulino et al.[5] where 99.4% is the reported accuracy. In this case wearable sensors are tested during the study including body postures apart from movements.

Siirtola and Röning compared k-nearest neighbour and quadratic discriminant analysis classifiers [6] with a fully embedded implementation on a smartphone adapted to its properties. They announced more than 99% success rate into recognizing the walking activity in real time and as low as close to 70% for other activities from both methods. Offline testing was also done and the rates were considerably lower.

In this paper a basic study is presented over the distribution of the raw accelerometer data – periodic samples along 3 main directions *x*, *y*, and *z* while performing 3 basic activities – running, walking, and sitting. Analyzing the dispersion of the input data allows to find the overlapping of the areas typical for the different activities and to suggest proper classifiaction approaches for further recognition. In Section 2 an algorithm for preprocessing and clustering of the raw data is described, followed by the experimental results obtained with a detailed discussion of what kind of additional processing would be needed and then in Section 4 a conclusion is made.

2. ALGORITHM DESCRIPTION

After reading the input raw data a separation is done over the matrix *A* containing the acceleration values over the three dimensions *x*, *y* and *z*. Then a

low-pass filtering is implemented over each of the series using a Butterworth filter. It was selected due to its maximally flat frequency response in the passband. The gain *G(ω)* of this filter in the general case of *n*-th order is represented by its transfer function *H(s)*:

$$G^2(\omega) = |H(j\omega)|^2 = \frac{G_0^2}{1 + \left(\frac{j\omega}{j\omega_C}\right)^{2n}}, \quad (1)$$

where ωc is the cutoff frequency at -3 dB; G_0 – the DC gain. The transfer function *H(s)* could be precisely determined by the following product having in mind the properties of the Laplace transform:

$$|H(j\omega)|^2 = H(s)H(-s) = \frac{G_0^2}{1 + \left(\frac{-s^2}{\omega_c^2}\right)^n}. \quad (2)$$

The final form of the system function can also be expressed using the poles:

$$H(s) = \frac{G_0}{\prod_{k=1}^{n}(s - s_k)/\omega_c}. \quad (3)$$

Thus, each vector along the different directions is filtered with the digitized form of this filter into the 1D-signal space. Then, the filtered samples are normalized within the range of [0, 1].

The next stage of the proposed algorithm include clustering of the already preprocessed data using the K-means approach. It is a kind of vector quantization where *n* registered values are split into *k* clusters. Inside each cluster falls a sample which is closest to its mean leading to partitioning of the inputs to Voronoi cells.

Following the steps of the algorithm the aim is to achieve:

$$\arg\min_S \sum_{i=1}^{k} \sum_{x \in S_i} \|x - \mu_i\|^2 = \arg\min_S \sum_{i=1}^{k} |S_i| VarS_i \quad (4)$$

where μ_i is the center from the multitude S_i. In other words it is necessary to minimize the squared deviations among adjacent points within one cluster:

$$\arg\min_S \sum_{i=1}^{k} \frac{1}{2|S_i|} \sum_{x,y \in S_i} \|x - y\|^2. \quad (5)$$

Since the cummulative deviation is fixed the inter-cluster squared deviations are going to be maximized as a result.

After the clustering the distribution of the formed groups is analyzed by plotting the scattering of vectors representing the accelerations.

3. EXPERIMENTAL RESULTS

Capturing the raw data is accomplished by the use of accelerometer embedded in an Android smartphone. The user can visualize all the parameter changes through application called Accelerometer Monitor. Selecting the option for record the information from the sensor is stored into the phone's memory in the following format:

Accelerometer Values
filename: default.txt
Saving start time: Wed May 13 19:32:17 GMT+01:00 2015
sensor resolution: 0.038300782m/s^2
#Sensorvendor: Bosch Sensortec, name: BMA250 Acclerometer, type: 1,version : 1, range 39.22
X value, Y value, Z value, time diff in ms

0.421 3.639 7.776 21
-0.114 3.639 7.967 20
-0.153 3.639 8.236 22
-0.114 3.677 8.427 19
-0.114 3.677 8.427 19
0.306 4.06 8.58 21
0.0 4.367 8.619 21
-0.076 4.405 8.81 19
-1.647 -0.574 9.959 20

end
#Wed May 13 20:03:39 GMT+01:00 2015

The first three columns are the acceleration values along the *x*, *y* and *z* axes, and the fourth is the time interval between the samples. The graphical user interface of the application is shown in Fig. 1-2.

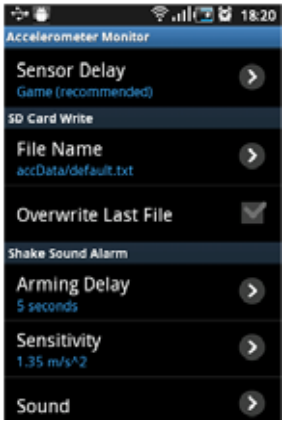

Figure 1. Main menu of the Accelerometer Monitor

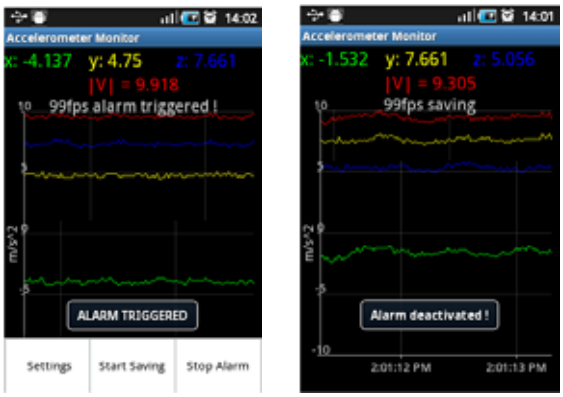

a) b)

Figure 2. Acceleration plots over three dimensions with a) alarm triggered and b) alarm deactivated

After the accumulation of all data a file is preserved for offline processing within the Matlab R2013A environment. It is run over IBM PC compatible computer with Intel CPU 2.8 GHz, 6 GB RAM under the control of MS Windows 7 Ultimate OS.

The source code of the main operations is given below:

```
clc
clear all
close all
fname='C:\Users\Pavel\Desktop\default.txt';% Loading the raw data from file
delim=' ';
A=importdata(fname,delim);

x=A(:,1);%Separating of the raw data matrix into vectors extracting the last fourth column
y=A(:,2);
z=A(:,3);
freq=50;%Sampling rate of the signal coming from the accelerometer
[b a] = butter(50,0.3,'low');% Low-pass filter design
x=filter(b,a,x);%Low-pass filtering for each signal separately
y=filter(b,a,y);
z=filter(b,a,z);
x=(x-min(x))/(max(x)-min(x));%Normalizing the data
y=(y-min(y))/(max(y)-min(y));
z=(z-min(z))/(max(z)-min(z));
A=cat(2,x,y,z);%Concatenating the vectors into a matrix for further clustering
[idx,c] =
kmeans(A,3,'distance','cityblock','Replicates',10);% Clustering the data with k-means
figure(1)
hold on
%plot(A(idx==1,1),A(idx==1,2),'r.','MarkerSize',12)
%3-D
%plot(A(idx==2,1),A(idx==2,2),'b.','MarkerSize',12)
% plot
%plot(A(idx==3,1),A(idx==3,2),'g.','MarkerSize',12)
%
plot3(A(idx==1,1),A(idx==1,2),A(idx==1,3),'r.','MarkerSize',12)       %2-D
plot3(A(idx==2,1),A(idx==2,2),A(idx==2,3),'b.','MarkerSize',12)       % plot
plot3(A(idx==3,1),A(idx==3,2),A(idx==3,3),'g.','MarkerSize',12)
plot3(c(:,1),c(:,2),c(:,3),'kx',...!
    'MarkerSize',15,'LineWidth',3)
legend('Running','Walking','Sitting','Centroids',...
      'Location','NW')
title 'Cluster Assignments and Centroids'
grid on;
hold off
```

The experimental results from executing the above code are given in Fig. 3-10. In Fig. 3 the 3-dimensional distribution of the vectors along the main spatial directions is given starting with *x* from the left. It is not symmetrical – the size of the volume occupied by the vectors representing the sitting (in green) is smaller than that of those for running (in red) and inbetween are the vectors for walking (in blue).

As expected, the sitting is characterized with smallest accelerations along all three directions, followed by the walking and highest values are obtained from registering the running. It's also observed that the deviation for the latter is greater varying from very low accelerations for the *y* and *z* directions up to very high ones. Along the *x* axis the effective corss section starts from mid-range magnitudes and goes up to some maximum high above any other activity.

The same behaviour of the vectors' scattering is established from the inverted representation shown in Fig. 4. There it can be seen that the deviation for the walking activity vectors, although a bit lower, is also considerable along the *y* and *z*. The most compact area is occupied by the recorded accelerations for sitting.

When taking into account the possibility of recognizing the different activities it becomes necessary to investigate the separability of the three clusters. In Fig. 5 a projection along *y* is depicted from the 3D distribution. The centers of the clusters are marked with 'x'-s. At this cale it seems that there is

good separability between the activities but the closer look suggests the opposite. As Fig. 6 reveals there is overlap with an average value of 0.02 in the normalized range of [0, 1] between sitting and walking. It happens along almost straight line as a boundary with a sharp jump area in the middle. A recommendation of using Support Vector Machine (SVM) into selecting the proper boundaries could be made at this point.

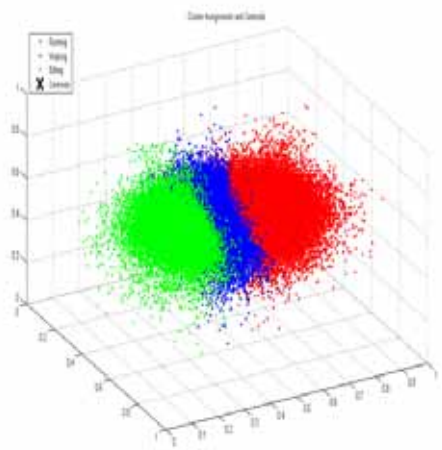

Figure 3

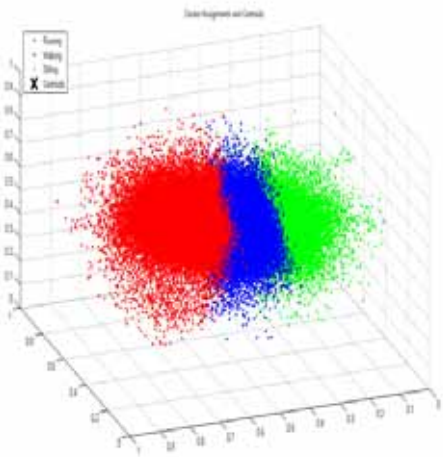

Figure 4

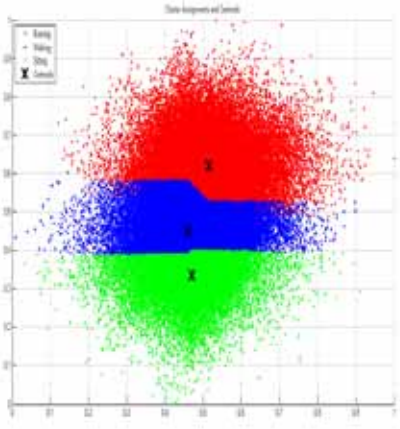

Figure 5

Similar is the case along the boundary between the walking and running activities (Fig. 7). Here, the overlapping is 0.04 on average at the same scale with an even higher jump, again around the middle of the border. Once more, SVM could be a proper solution for the case.

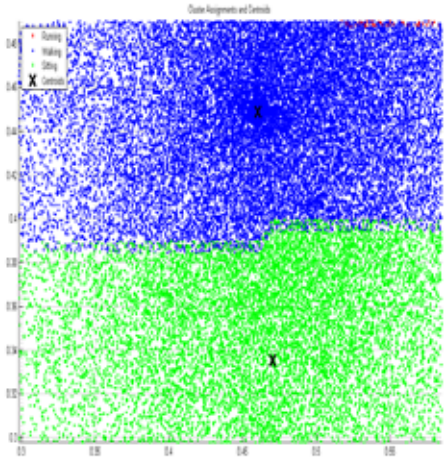

Figure 6

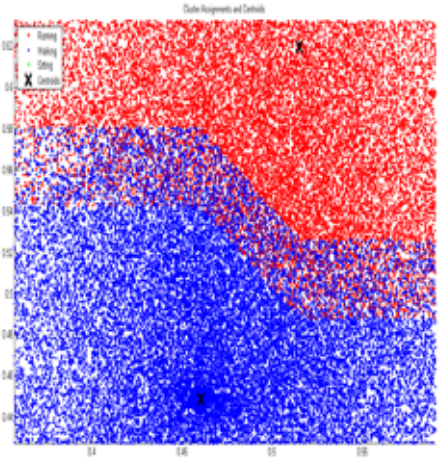

Figure 7

In Fig. 8 both the boundaries are visible at greater magnifying level in an area where the jumps are not persisting but still the overlapping is considerable. The diffusion of vectors is less dense between the sitting and walking areas at both ends of the clusters.

Almost the same is the dissipation between running and walking at the lower endbut considerably higher density is observed for these activities at the upper limit, typical for the central parts as well.

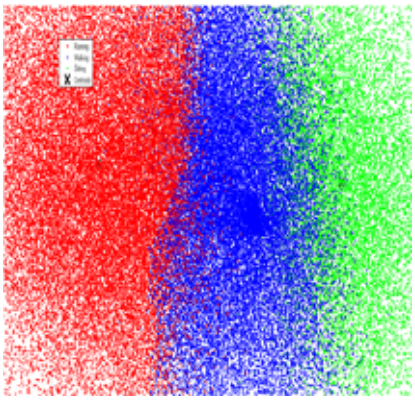

Figure 8

4. CONCLUSION

The use of accelerometer data for human activity recognition is very convenient because there are quite widespread and cheap sensors. But the processing can be difficult because the signals that are received in the individual activities are highly correlated with each other. There is a need for better classification methods that will inevitably require more time for calculation and more power from the device which can be problematic with mobile ones. All data used in the current study is collected from just one subject. The results are obtained independently.

The application of the proposed approach has its broad potential users, e.g. for elderly or sick people it is possible to calculate the distance travelled or the time spent sitting and being informed that they have not moved enough during the day and have to catch up. It can also be used by active sportspeople who want to keep track of how far they've gone as a distance or how long they have done.

Acknowledgements

This work was supported by the National Scientific Fund at the Ministry of Education and Science, Republic of Bulgaria, within the project DFNI I02/1 "Intelligent man-machine interface for assistive medical systems in improving the independent living of motor disabled users".

References

[1] Ghosh, Arindam; Riccardi, Giuseppe. Recognizing human activities from smartphone sensor signals. In: Proceedings of the 22nd ACM international conference on Multimedia. ACM, 2014. p. 865-868.

[2] Ronao, Charissa Ann; Cho, Sung-Bae. Human activity recognition with smartphone sensors using deep learning neural networks. Expert Systems with Applications, 2016, 59: 235-244.

[3] Ronao, Charissa Ann; Cho, Sung-Bae. Human activity recognition using smartphone sensors with two-stage continuous hidden Markov models. In:Natural Computation (ICNC), 2014 10th International Conference on. IEEE, 2014. p. 681-686.

[4] Ronao, Charissa Ann; Cho, Sung-Bae. Deep convolutional neural networks for human activity recognition with smartphone sensors. In: International Conference on Neural Information Processing. Springer, Cham, 2015. p. 46-53.

[5] Ugulino, Wallace, et al. Wearable computing: Accelerometers' data classification of body postures and movements. Advances in Artificial Intelligence-SBIA 2012, 2012, 52-61.

[6] Siirtola, Pekka; Röning, Juha. Recognizing human activities user-independently on smartphones based on accelerometer data. International Journal of Interactive Multimedia and Artificial Intelligence, 2012, 1.5.

[7] Shoaib, Muhammad; Scholten, Hans; Havinga, Paul JM. Towards physical activity recognition using smartphone sensors. In: Ubiquitous Intelligence and Computing, 2013 IEEE 10th International Conference on and 10th International Conference on Autonomic and Trusted Computing (UIC/ATC). IEEE, 2013. p. 80-87.

[8] Su, Xing; Tong, Hanghang; Ji, Ping. Activity recognition with smartphone sensors. Tsinghua Science and Technology, 2014, 19.3: 235-249.

EM EXPOSURE STUDY OF A HUMAN INSIDE THE CAR

Veriko Jeladze, Tamar Nozadze, Vasil Tabatadze, Ivan Petoev, Revaz Zaridze

Tbilisi State University, Laboratory of Applied Electrodynamics and Radio Engineering
3, Chavchavadze Ave. 0176, Tbilisi, Georgia

E-mail: veriko.jeladze001@ens.tsu.edu.ge,
E-mail: tamar.nozadze002@ens.tsu.edu.ge

Abstract

The goal of the proposed research is to investigate the influence of mobile phone's EM Radiation on a human, when it is located inside the car and study possible resonant fields in cars. We have investigated several cases when a human with a cellphone is located inside a car and also the case when the EM source is the base station antenna located outside, at 450 MHz, 900 MHz and 1800 MHz frequencies. The problems are solved using the Method of Auxiliary Sources (MAS). The numerical results showed the presence of resonance phenomena and high reactive field (standing waves) in several scenarios, that causes higher SAR in human tissues and could be dangerous for a human.

1. INTRODUCTION

Nowdays it's especialy important and actual to investigate the impacts of electromagnetic fileds (EMF) emitted from the cellphones and other wireless communication devices on human. The interaction between the EMFs and the biological object depends on the characteristics of the emitting source, as well as the ability to absorb and accumulation energy by biological organisms. Many publications show that absorption of radiated energy (SAR) depends on mobile phones and antenna types [1, 2], its positions, and radiated power from the mobile phones [3]. The radiation nature and EM fields behavior depends on complex human body geometry [4], user hand and fingers positions [2, 5], other subjects' existence around the user, etc. It's also important to consider where the user is located, in an enclosed or semi-enclosed space (room, car, etc.). But it's impossible to thoroughly quantitatively consider all these details.

In our previous works [6, 7] we have investigated the cellphone's antenna and base station's radiation influence on the user located inside the room with a window. The studies were conducted by the Method of Auxiliary Sources (MAS), which was also used to simulate room walls with different transparency. The results showed the presence of high reactive fields in the room with less walls transparency [7].

In this paper our goal is to investigate mobile phones antenna EM exposure influence on a human, when person is located inside the car and study possible resonant fields in cars at 900 MHz and 1800 MHz radiation frequencies. The motivation of this research is that we often use mobile phones and other handsets in a car (e.g. walkie-talkies are used in police cars). As it is known, cars are made using metal and other conductive materials, which are less transparent to EM waves. At some frequencies in the mobile frequency range, this closed metal structure behaves as a resonator and amplifies the antenna radiated near field, which becomes dangerous for the user. Besides, the novelty in the proposed research is the ground effect consideration under the car, as a reflective surface. It is also important to study SAR distributions inside the human body and investigate the fields' behavior in the near and far zone.

There are some publications [8-9] similar to the stated problem solved by different numerical methods, but we suppose that, the EMF exposure influence on a human inside the car is not studied completely yet.

2. MATHEMATICAL APPROACH AND METHODOLOGY

We consider the system model which consists of the car and human inside it. The system is irradiated by the known EM wave, which is located inside the car as a mobile phone antenna. Our goal is to find the EMF distribution inside and outside the car and also, inside a human body and also to investigate the earth surface influence on the resonant field formation inside the car. In the considered model (Figure 1) the car represents the perfectly conductor surface S. On these surface there are

open parts like windows σ_w, $w = 1, 2, \ldots$ - number of glasses. As a human model we use the homogenous dielectric model of a human shape "Mummy" with averaged permittivity and losses [6], which is bounded with the closed surface S_0.

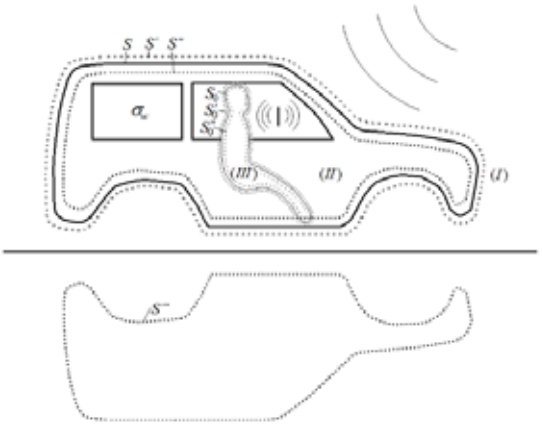

Figure 1. MAS model of cavity with using auxiliary surfaces

The irradiated fields of the inner source $\vec{E}^1_{inc}, \vec{H}^1_{inc}$ (first case) and the field of the outer source $\vec{E}^2_{inc}, \vec{H}^2_{inc}$ (second case) are initially given. We have to determine the field in three areas: (I) outside the car, (II) inside car, (III) inside human (Figure 1). We denote these fields correspondingly $\vec{E}_{(I)}, \vec{H}_{(I)}$, $\vec{E}_{(II)}, \vec{H}_{(II)}$, $\vec{E}_{(III)}, \vec{H}_{(III)}$. The stated problem is solved numerically, using the Method of Auxiliary Sources (MAS).

For this reason we construct two couples of auxiliary surfaces: S_0', S_0'' - outside and inside human, and S', S'' – outside and inside car, where the auxiliary sources are distributed. As the auxiliary sources two mutual perpendicularly oriented combined dipoles (Huygens source) [10, 11] with unknown amplitudes are used. The electric and magnetic field of the combined dipole we denote as:

$$\vec{G}_E \to \vec{G}_E\left(\vec{r}, \vec{r}_0, \vec{p}_e, \vec{p}_h, \varepsilon, \mu\right),$$
$$\vec{G}_H \to \vec{G}_H\left(\vec{r}, \vec{r}_0, \vec{p}_e, \vec{p}_h, \varepsilon, \mu\right), \qquad (1)$$

Where $\vec{r}$ and $\vec{r}_0$ are the observation point and dipole location point radius-vectors, $\vec{p}_e$ and $\vec{p}_h$ – are the unit vectors of the electric and magnetic dipole polarization, ε and μ-are media parameters. In order to describe the scattered field of any polarization, in each point of the auxiliary surface we consider two such dipoles, distributed in the tangent plane and rotated by 90^0 to each other. Respectively, for electric and magnetic field of the auxiliary source we have:

$$A_0\vec{G}_E + B_0\vec{G}'_E, \quad A_0\vec{G}_H + B_0\vec{G}'_H \qquad (2)$$

Where: $\vec{G}'_E \to \vec{G}_E\left(\vec{r}, \vec{r}_0, \vec{p}'_e, \vec{p}'_h, \varepsilon, \mu\right)$, $\vec{p}'_e = \vec{p}_h$, $\vec{G}'_H \to \vec{G}_H\left(\vec{r}, \vec{r}_0, \vec{p}'_e, \vec{p}'_h, \varepsilon, \mu\right)$, $\vec{p}'_h = -\vec{p}_e$, A_0 and B_0 are unknown complex amplitudes, which can be determined by satisfaction of the the corresponding boundary conditions.

The field in the first (I) area is the sum of the incident field $\vec{E}^1_{inc}, \vec{H}^1_{inc}$ and the field described by the auxiliary sources on the surface S''. The field in the second (II) area is the sum of the incident field $\vec{E}^2_{inc}, \vec{H}^2_{inc}$ and the fields described by the sources located on the surface S' and S_0''. In the third (III) area the field is described by the sources on the surface S_0' (Figure 1). Therefore:

$$\vec{E}_{(I)}\left(\vec{r}\right) = \vec{E}^1_{inc}\left(\vec{r}\right) + \sum_{n=1}^{N}\left[A_n\vec{G}_E + B_n\vec{G}'_E\right]_{\vec{r}_n \in S''} \qquad (3)$$

$$\vec{E}_{(II)}\left(\vec{r}\right) = \vec{E}^2_{inc}\left(\vec{r}\right) + \sum_{n=1}^{N}\left[C_n\vec{G}_E + D_n\vec{G}'_E\right]_{\vec{r}_n \in S'} + \sum_{m=1}^{N_0}\left[E_m\vec{G}_E + F_m\vec{G}'_E\right]_{\vec{r}_m \in S_0''} \qquad (4)$$

$$\vec{E}_{(III)}\left(\vec{r}\right) = \sum_{m=1}^{N_0}\left[K_m\vec{G}_E + L_m\vec{G}'_E\right]_{\vec{r}_m \in S_0'} \qquad (5)$$

$$\vec{H}_{(I)}\left(\vec{r}\right) = \vec{H}^1_{inc}\left(\vec{r}\right) + \sum_{n=1}^{N}\left[A_n\vec{G}_H + B_n\vec{G}'_H\right]_{\vec{r}_n \in S''} \qquad (6)$$

$$\vec{H}_{(II)}\left(\vec{r}\right) = \vec{H}^2_{inc}\left(\vec{r}\right) + \sum_{n=1}^{N}\left[C_n\vec{G}_H + D_n\vec{G}'_H\right]_{\vec{r}_n \in S'} + \sum_{m=1}^{N_0}\left[E_m\vec{G}_H + F_m\vec{G}'_H\right]_{\vec{r}_m \in S_0''} \qquad (7)$$

$$\vec{H}_{(III)}\left(\vec{r}\right) = \sum_{m=1}^{N_0}\left[K_m\vec{G}_H + L_m\vec{G}_H\right]_{\vec{r}_m \in S_0'} \qquad (8)$$

In the given expression there are unknown complex amplitudes A_n, B_n, C_n, D_n, E_m, F_m, K_m L_m of the auxiliary sources, the total number of which is $4 \cdot \left(N + N_0\right)$. These amplitudes can be determined from the boundary conditions. On the surface S as on the conductor, the tangent components of the complete fields $\vec{E}_{(I)}$, $\vec{E}_{(II)}$ must be zero; On the windows surfaces σ_w and human

model surface, as on the dielectric, the tangent components of the fields $\vec{E}_{(I)}, \vec{E}_{(II)}, \vec{H}_{(I)}, \vec{H}_{(II)}$ and $\vec{E}_{(II)}, \vec{E}_{(III)}$, $\vec{H}_{(II)}, \vec{H}_{(III)}$ must be continuous. As a result, we get the system of the linear algebraic equations to the unknown amplitudes. After solution of this system using the computer numerically, the unknown fields are determined in all given areas.

As it was mentioned above, the big interest is to investigate the ground surface influence on the fields formation. We suppose that the ground surface is perfect planar conductor. This gives ability to use the method of the mirror image in order to describe the reflected field. The consideration of the reflected field adds the additional terms in the expressions (3) and (6) for the field in the first area. As for the fields in the second and third areas the reflected field changes only the amplitudes of the auxiliary sources.

According to the MAS, towards ground there is constructed the mirror image S''' of the surface S'' (Figure 1). The amplitudes of the auxiliary sources on the surface S''' differs from the corresponding sources on the surface S'' only by sign as it is in case of the mirror image. In the other words the consideration of the ground surface doesn't change the number of the unknown coefficients. The field in the first area has the form:

$$\vec{E}_{(I)}(\vec{r}) = \vec{E}^1_{inc}(\vec{r}) + \sum_{n=1}^{N}\left[A_n\vec{G}_E + B_n\vec{G}'_E\right]_{\vec{r}_n\in S'''} + \\ + \sum_{n=1}^{N}\left[(-A_n)\vec{G}^*_E + (-B_n)\vec{G}'^*_E\right]_{\vec{r}_n\in S'''} \quad (9)$$

$$\vec{H}_{(I)}(\vec{r}) = \vec{H}^1_{inc}(\vec{r}) + \sum_{n=1}^{N}\left[A_n\vec{G}_E + B_n\vec{G}'_E\right]_{\vec{r}_n\in S'''} + \\ + \sum_{n=1}^{N}\left[(-A_n)\vec{G}^*_E + (-B_n)\vec{G}'^*_E\right]_{\vec{r}_n\in S'''} \quad (10)$$

The unknown amplitudes are again determined from the boundary conditions.

3. RESULTS OF NUMERICAL SIMULATIONS AND DISCUSSIONS

Based on above proposed methodology (MAS), we have created program package and investigated several exposure scenarios. Calculations were carried out at 900 and 1800 MHz radiation frequencies. EM source is placed at 2.5 cm distance from the human head. The car has following dimensions (LWH): 4.10 x 1.76 x 1.57 [m].

For all results near and far field values are given in the relative units, whereas point SAR values are provided in W/Kg and normalized to 1 W input power.

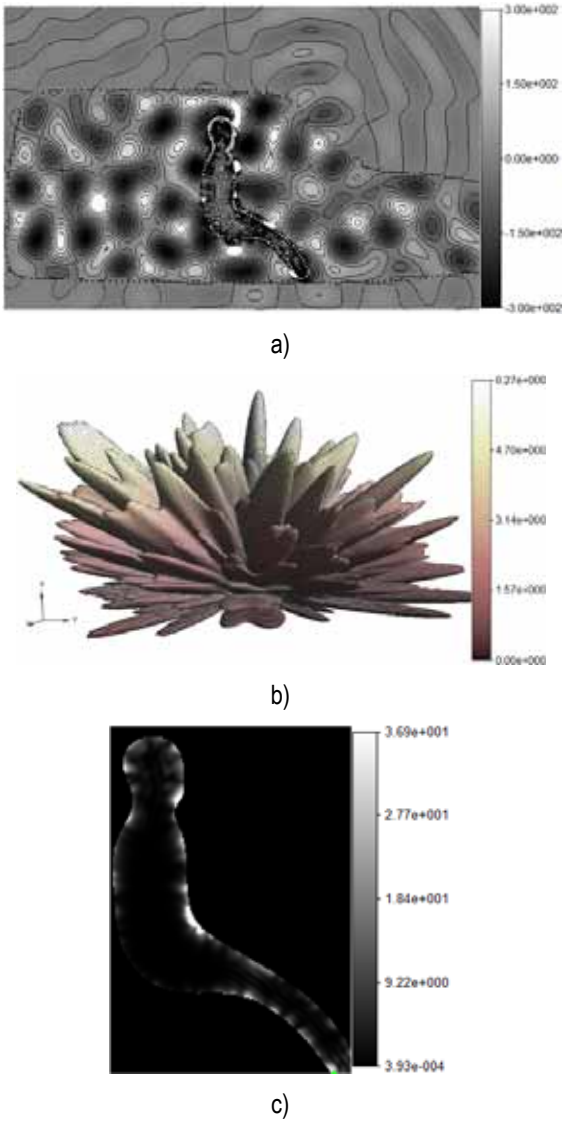

Figure 2. Near field distribution in XOZ plane inside the car (a), far field pattern (b) and point SAR distribution (W/Kg) for the human body (c) at 900 MHz.

On Figures 2 (a, b, c) near field distribution inside the car in XOZ section and far field pattern and point SAR distribution for the human body at 900 MHz frequency are presented respectively. In this case point SAR peak value is 36.9 W/Kg. The wavelength is smaller than car window size and radiated energy penetrates inside the car though the side windows mainly. Standing waves are observed in the back part of car. The bottom of pattern shape is flat, which is caused by the field reflection

and propagation over the ground surface under the car.

We have investigated car's resonant properties and generate resonant characteristic near to the 900 MHz frequency. Figure 3 shows the detailed frequency characteristic on which we see the sharp, discriminated resonance frequency 899.9 MHz.

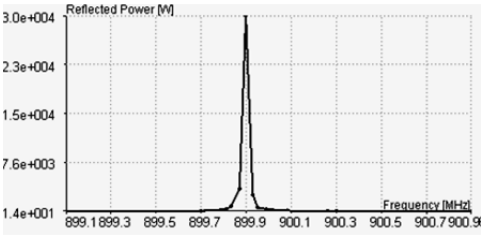

Figure 3. Frequency characteristic for the car with human model inside, near to 900 MHz

Figure 4 shows near field inside the car (a) and point SAR distribution for the human body (b) at 899.9 MHz resonant frequency. As it seen from the obtained result inside the car is created high reactive field and the point SAR peak value is about ten times higher than it was for the 900 MHz frequency.

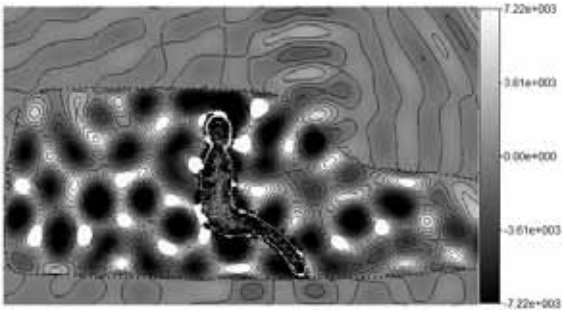

a)

b)

Figure 4. Near filed distribution inside the car (a) and point SAR (b) distribution for the human body at 899.9 MHz resonant frequency

We have also studied the near field distribution inside the car at 1800 MHz (Figure 5). Because of the high losses at this frequency the depth of the field penetration in the human model is smaller than for the lower frequencies and EM field absorption occurs mostly in the skin layer.

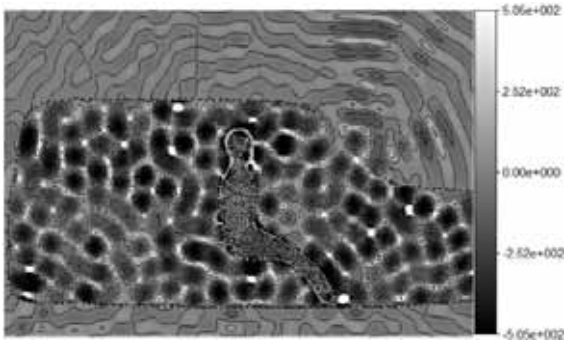

Figure 5. Near field distribution in the car at 1800 MHz frequency (source is base station antenna).

On Figure 6 are presented the SAR values inside the human body, when it is located in free space and in the car, at 450, 900 and 1800 MHz frequencies. We see that in the car these values for the human body is almost 4 times higher than in free space, which can be dangerous for the human.

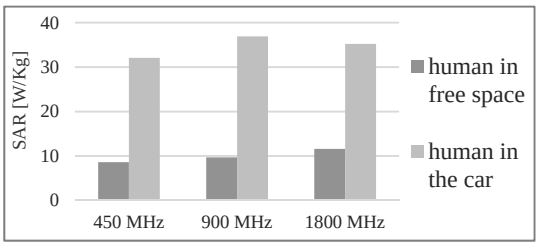

Figure 6. Point SAR values for the human body, when EM source is near the head.

We have also considered the case, when the ground effect under the car isn't taking into account. In this case the field values inside the car is lower (Figure 7) than in case when we consider this effect (Figure 2a).

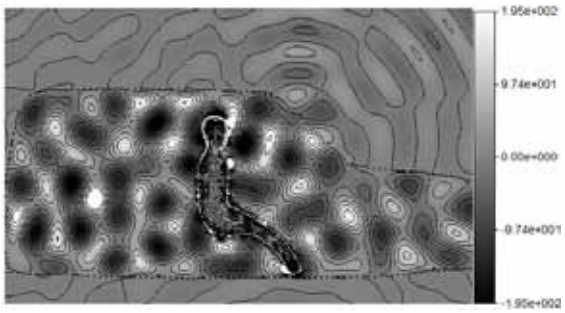

Figure 7. Near field distribution in XOZ plane inside the car without considering ground effect at 900 MHz

For all obtained above results calculation error was less than 20%.

4. CONCLUSION

The mobile phone's EM exposure problem for a human model located in the car is studied using the Method of Auxiliary Sources. This method was also used to simulate ground reflective surface. The obtained results, conducted with the MAS based program package, showed the presence of resonance and reactive fields inside the car, that causes high SAR in human tissues. It was shown that these SAR values is much higher than in case, when human is in free media. The reason of this is that at the considered frequencies car's metallic surface acts as the resonator. So it isn't desirable speak on phones for a long time inside the car, that can be hazardous for the cellphone users.

5. ACKNOWLEDGMENT

This study is supported by Shota Rustaveli National Science Foundation grant: YS15_2.12_56.

References

[1] M. R. I. Faruque, et al.,"Effects of dielectric values& substrate materials on electromagnetic (EM) absorption in human head," Frequenz Journal, vol. 66, no. 3-4, pp. 79-83, 2012.

[2] J. Keshvari & M. Kivento, "Hand Effect on Head Specific Absorption Rate (SAR) Exposed by Two Realistic Phone Models," in Radio and Antenna Days of the Indian Ocean (RADIO 2012), IOP Conf. Series: Materials Science and Engineering, 2012.

[3] J. Wiart et al., "Analysis of the influence of the power control and discontinuous transmission on RF exposure with GSM mobile phone," IEEE Trans. on Electromag. Compat., vol. 42, no. 4, pp. 376-385, 2000.

[4] M. R. I. Faruque, et. al, "Effect of human head shapes for mobile phone exposure on electromagnetic absorption," Journal of Microelectronics, Electronic Components and Materials, vol. 40, no. 3, pp. 232-237, 2010.

[5] V. Jeladze, M. Tsverava, T. Nozadze, et al., "EM Exposure Study on Inhomogeneous Human Model Considering Different Hand Positions," XXI-th Int. Seminar/Workshop on Direct and Inverse Problems of EM and Acoustic Wave Theory (DIPED-2016), Tbilisi, Georgia, September 26-29, 2016.

[6] V. Jeladze, I. Petoev, V. Tabatadze, M. Prishvin, R. Zaridze, "Application of the Method of Auxiliary Sources to Study the Influence of Resonance Electromagnetic Fields on a Man in Large Spatial Domains," Journal of Commun. Technology and Electronics, vol. 62, no. 3, pp. 195-204, March 2017.

[7] V. Jeladze, V. Tabatadze, M. Prishvin, I. Petoev, R. Zaridze, "Influence of the Walls Transparency on the Resonant EM Field's Values," Journal of Applied Electromagnetism (JAE), vol. 18, no. 1, pp. 1-13, June 2016.

[8] G. Anzaldi, et al., "Initial Analysis of SAR from a Cell Phone Inside a Vehicle by Numerical Computation," IEEE Trans. on Biomed. Eng, vol.54, no.5, pp.921-930, May 2007.

[9] A. Dhami, "Studies on Cell-phone Radiation Exposure Inside a Car and Near a Bluetooth Device," Int. J. Environ. Res., vol. 9, no. 3, pp. 977-980, Summer 2015.

[10] В. В. Никольский, Электродинамика и распространение радиоволн, М.: Наука, 1978, p. 221.

[11] I. M. Petoev, V. A. Tabatadze, R. S. Zaridze, "The Method of Auxiliary Sources Applied to Problems of Electromagnetic Wave Diffraction by Certain Metal–Dielectric Structures," Journal of Commun. Techn. and Electronics, vol. 58, no. 5, pp. 404-416, 2013.

THE EFFECT OF WEATHER ON QUALITY OF EXPERIENCE IN OPTICAL WIRELESS COMMUNICATION SYSTEM

Rasa Bruzgiene[1], Lina Narbutaite[2], Erich Leitgeb[3], Pirmin Pezzei[3], Thomas Plank[3]

[1]Department of Telecommunications, Kaunas University of Technology
[2]Department of Software Engineering, Kaunas University of Technology
Kaunas, Lithuania

[3]Institute of Microwave and Photonic Engineering, Graz University of Technology
Graz, Austria

E-mail: rasa.bruzgiene@ktu.lt

Abstract

Optical Wireless communication systems are a good competitor to other wireless communication technologies in relation of its capacity to deliver high-speed broadband traffic. The way optical wireless transceivers operate is more or less the same as fiber optics ones; however, since laser signals are transferred through the atmosphere, the path loss between the transmitter and the receiver is getting raised due to various external factors (conditions) that appear on weather. The characteristics of optical wireless systems and it changes in the face of different weather conditions strongly affect the parameters of Quality of Service. Also, this influence provides the possibility to quantify the significance of the service disruption impact to the metrics of Quality of Experience. Due to this, this paper gives a new approach to the relation of the characteristics of optical wireless communication system, known as Free Space Optics, affected during the weather-based disruptions with the parameters of Quality of Service. Furthermore, this relation is used in estimation of Quality of Experience metrics.

1. INTRODUCTION

Optical Wireless (OW) systems are the good example of the integration between optical and wireless radio communications, where the light of different types is caring the main signal for data transmission over the atmospheric channel. The basic Optical Wireless system consists of three main parts (Fig. 1) - source system (optical transmitter, a modulator and an irradiation device – a telescope or a lens), channel for signal transmission and receiver system (a detector, a decoder, and a telescope or a lens).

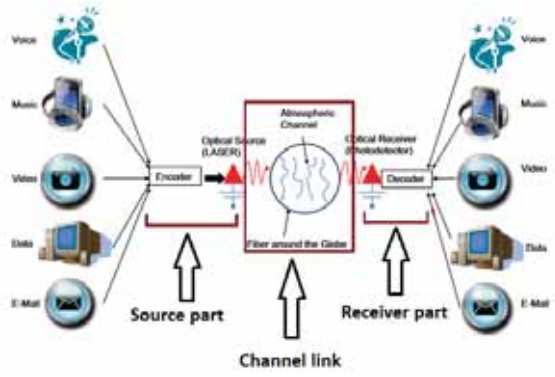

Figure 1. Structure of Optical Wireless communication system [modified from [1]]

In OW system, the information from the optical transmitter is modulated on a collimated beam of light, which is projected through free air channel onto the receiver side [1]. The channel for signal transmission is a free space (air). Since the medium for signal carrier is a light, such system operating frequencies are very high and range from 300 GHz to 300 PHz. It includes infrared (750 nm – 1mm), visible (390-750 nm) and ultraviolet bands (200-280 nm) [2]. Due to this, Optical Wireless communication can be classified into Free Space Optics (FSO), Visible Light Communication (VLC) and Ultraviolet Communication (UVC). FSO, known as terrestrial point-to-point OW communication system, offers a cost-effective protocol-transparent link with high data rates (as 10 Gbps per wavelength). Such system allows to set up communication links between two locations whenever a free line of sight is present [2]. Typical wavelength of Free Space Optics system ranges from 800 to 1700 nm. For this reason, Optical Wireless communication system can be used in cellular backhauls, wireless MAN extensions, WLAN-to-WLAN connectivity in different environments, broadband access to remote or underserved areas [2] and *etc.* Also, Optical Wireless system can be used not only for temporal installations, but as well in the face of a crisis for emergen-

cy and medical needs or permanent connections in last mile access without cabling.

However, a key disadvantage of Optical Wireless systems is it sensitivity to atmospheric conditions and limited reliability. The resilience of such systems against fast-time-changing disruptions is dependent to different weather conditions as fog, snow, rain, clouds and *etc*. In general, for a higher resilience of such systems it is important to identify the appropriate acceptable level of service over weather-based disruptions. Acceptable level of service can be refined based on the service disruption impact to a user. And the Quality of Service and Quality of Experience plays a key role in this way.

The paper is organized as follows. Section 2 describes investigations in order to analyze the impact of different weather conditions to the links of Optical Wireless System. Section 3 gives the solution for the correlation of optical wireless signal attenuation during the different weather conditions (with main focus to fog and clouds) to the bit error rate parameter during the service transmission over Optical Wireless system. The results from the correlation will be used as a main input for evaluation of the objective Quality of Experience metrics in Section 4. Finally, section 5 presents the conclusions and recommendations for further investigations.

2. IMPACT OF DIFFERENT WEATHER CONDITIONS TO OW LINKS

The atmosphere is composed of gas molecules, water vapor, aerosols, dust and pollutants, whose sizes are comparable to the wavelength of a typical optical carrier affecting the carrier wave propagation not common to a radio frequency (RF) system [2]. Absorption and scattering due to particulate matter may significantly attenuate the transmitted optical signal, while the wave-front quality of a signal-carrying laser beam transmitting through the atmosphere can be severely degraded, causing intensity fading, increased bit error rates, and random signal losses at the receiver. Due to this, the atmospheric channel for signal propagation over FSO communication has to deal with many external factors related to the different weather conditions [3]: rain, fog, sleet, snow, smog, clouds, different kinds of aerosols, variations in temperature and etc. All these weather conditions affect the wireless systems and Optical Wireless systems as well. It is just a difference in a scale of the affect to the parameters of OW communication performance.

The research group of the Institute of Microwave and Photonic Engineering in TU-Graz (Austria) has done a lot of work by investigating the impact of different weather conditions to the Optical Wireless communication, especially Free Space Optics systems. One test of their many investigations was done with a Multi-beam system [4]. This system was installed to connect the Department of Communications and Wave Propagation to the „Observatory Lustbühel" [5]. Figure 2 shows a terrain profile of this system [5]. The distance between FSO units was 2.7 km.

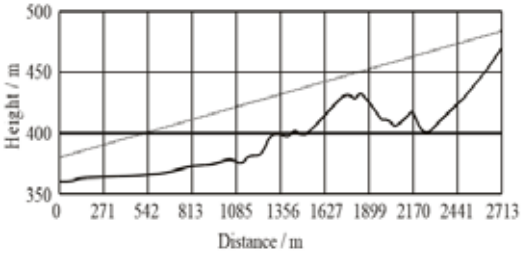

Figure 2. Terrain profile of FSO system [5]

Test data at 155 Mbps was sent from one FSO-unit to a distant FSO-unit. The received data was sent back (loop) to the first unit. As a reference to the link quality, weather data was recorded (including temperature, humidity, wind speed and direction and rain rate). The authors in this work [4] stated, that the main cause for failure of FSO links was fog. The same reason for OW system vulnerability was found in other investigation [6], comparing the fog attenuation for 850 and 950 nm wavelength in FSO system (Fig. 3).

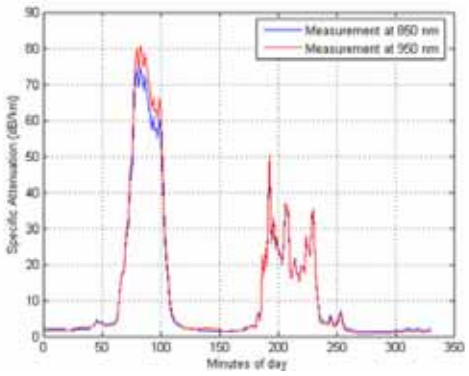

Figure 3. Influence of fog [6]

In generally, fog and water clouds mostly affect FSO links due to the size of it droplets. The size of droplets is of the same order of magnitude as wavelength, which implies a high extinction efficiency, and their concentration is much larger than the one of rain or snow.

Rain is also an important attenuator for the optical signals. Figure 4 shows that in period of a drizzle the mean power was decent by 2.5 dB at a rain rate of 2 mm/h.

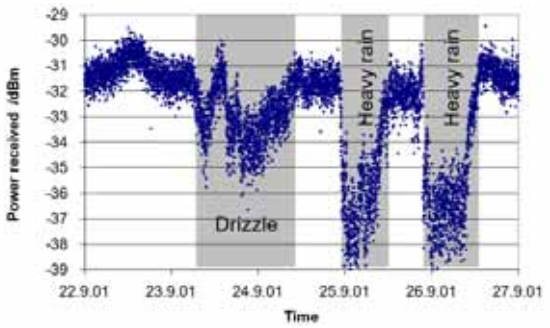

Figure 4. Influence of rain [7]

At the start of heavy rain with an average rain rate of 5 mm/h, accordingly the received power decent by 6 dB [7].

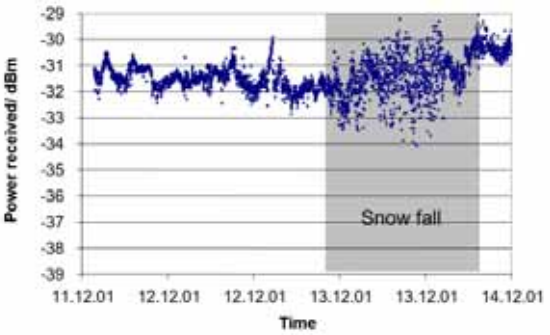

Figure 5. Snow influence [7]

Snow is usually constituted by aggregates of ice crystals and snowflakes have irregular shape or different compositions. A laser attenuation by falling snow can exceed 40 dB/km, depending on water content of snowflakes and on precipitation rate. In the investigation [7], which results are presented in Fig. 5, the received mean power of OW link stays unchanged, but the variance is increased significantly.

3. CORRELATION BETWEEN OPTICAL WIRELESS SIGNAL ATTENUATION AND QOS/QOE

As we can see in the previous section, performances characteristics of a data over FSO links depend upon the atmosphere in which it propagates. Each wireless channel has a computable Bit Error Rate (BER), which is the probability of the occurrence of an error during data transfer over that link. As fog mostly affects the quality of FSO links comparing to other weather conditions as a rain or a snow, further investigations were focused just on it effect.

Visibility is one of the parameters, which describes fog. The specific attenuation for both Kim and Kruse model is given by common empirical model [8]

$$\alpha(\lambda) = \frac{3.19}{V}\left(\frac{\lambda}{550}\right)^{-\gamma}, \quad (1)$$

where λ is operating wavelength (nm), V is stands for visibility range(km), γ is indicating the atmospheric attenuation coefficient according Kim or Kruse model.

The BER calculation are given by formula

$$BER = \frac{1}{2} erfc\left(\frac{1}{2}\sqrt{SNR}\right). \quad (2)$$

Quality assessment was carried out using SNR BER and MOS indicators, calculated by using hardware and software tools. Empirical values of BER transitions from an acceptable quality to the poor, according to the relationship between SNR and MOS, are presented in Table 1 [9].

For the evaluation of BER influence to QoS/QoE, we simulated two different types of fog (thick (0.2 m of visibility) and moderate (0.8 m of visibility) for two wavelengths: 1550 nm and 830 nm.

Table 1. Relationship between SNR BER and MOS [9]

MOS(%)	BER	SNR
100-81	$<10^{-8}$	>37
80-61	$10^{-8} < x < 10^{-6}$	31-37
60-41	$10^{-6} < x < 10^{-4}$	25-31
40-21	$10^{-4} < x < 10^{-2}$	20-25
<20	$>10^{-2}$	<20

We choosed these parameters, because the main idea was to evaluate QoE for several types of information: image and data.

4. EVALUATION OF OBJECTIVE QOE METRICS

The simulation was done using Matlab2017a software. At first, we calculated received power and BER. The results are presented in the Figures 6 and 7.

It can be seen, that the impact of the fog to OW link depends on the length of waves over FSO system. The shorter wavelength in OW link gives a possibility to transmit service of a good quality at least ~100 meters further during a thick or moderate fog.

The lines on the different BER values presents a level of perceived QoE by the user.

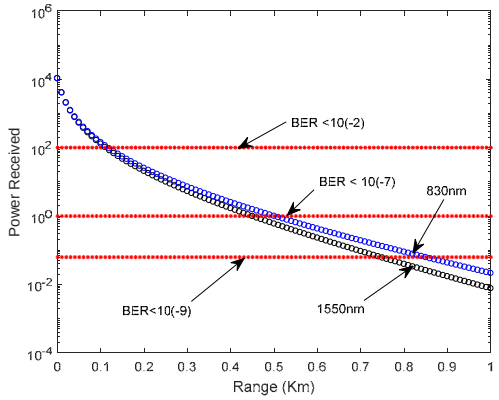

Figure 6. Thick fog

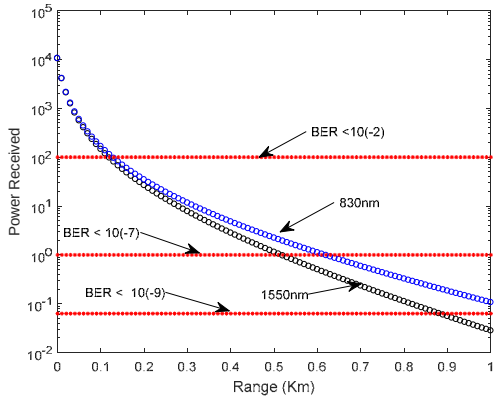

Figure 7. Moderate fog

The results in Figure 8 showed, what range we need to have SNR (or E_b/N_0) for different BER values.

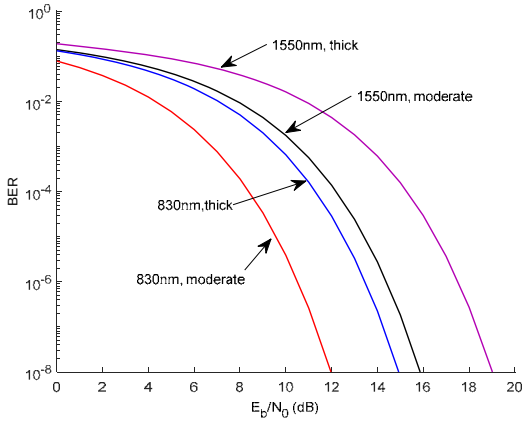

Figure 8. Relationship between BER and SNR

For evaluation of MOS and QoE was used image and data information. The simulation was done for QAM-126 modulation, and SNR was between 4 and 27 dBm. The image simulation results are presented in the Fig. 9-10.

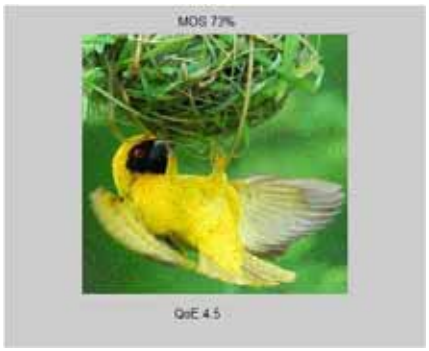

Figure 9. Relationship between MOS and QoE according BER

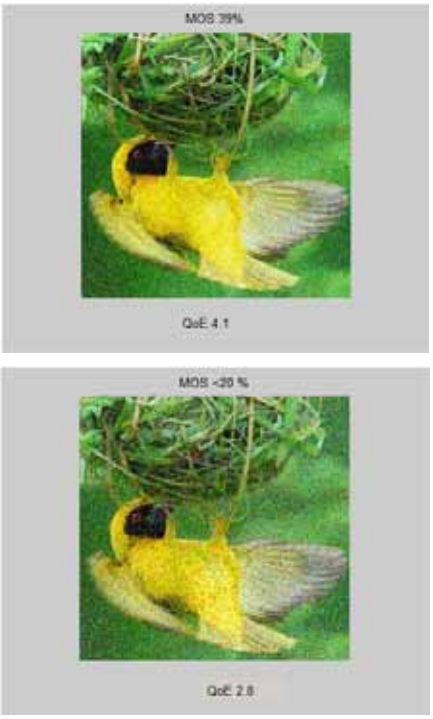

Figure 10. Relationship between MOS and QoE according BER

The data simulation results are presented in the Tables 2 and 3.

Table 2. Original information, which was sent

#5+BDC123245798BDC123245798BDC123245798zxcvbnm

Table 3. Received data

BER	MOS	QOE	Received data
$<10^{-2}$	<20	1.3	%»JCtq45718B DÃ527r4° DS1r #2>4792j:cfBnm
$<10^{-6}$	<37	3.6	"5+BEG123"457 9<BDÓ123r4571 YBLC10#245w98 zxcvbnm'
$<10^{-9}$	<92	4.9	#µ+BDC1232457 98BDC12324579 8BDC123245798 zxcfbnm

According to the obtained results in Figure 8 and in Table 3, it is seen, that the higher the error rate during the transmission process, the lower the QoS and QoE parameters for different types of information (in our case for image and data). In this way, the influence of different intensity fog can cause the vulnerability in Optical Wireless system parameters, but the user can still use the different type of services, just with the different affect to real perceived quality.

5. CONCLUSIONS

The investigations showed, that using of shorter wavelengths can increase the resilience of OW systems during the fog. Also, it is a big difference in the scale of fog influence to a different type of services, which are transmitted over OW link. If the user receives a data, the intensive fog can cause a big impact to the perceived quality of such service. However, if the user is using video service, he can feel just some single failures, but the service will be still in performance. The reason is a lower correlation between MOS and QoE. Due to this, a time interval occurs when the user sees the faults, but the service still can be used, even though that parameters of OW system starts to deteriorate. The main results from these investigations will help in further authors' work by creating a solution for an alert in order to react and prevent service performance degradation under the weather-based disruptions over wireless systems.

Acknowledgment

This article is based upon work from COST Action CA15127 ("Resilient communication services protecting end-user applications from disaster-based failures — RECODIS") supported by COST (European Cooperation in Science and Technology).

References

[1] Majumdar, Arun K., "Advanced Free Space Optics (FSO): A Systems Approach", New York, USA, Springer, 2015.

[2] Uysal, M., Capsoni, C., Ghassemlooy, Z., Boucouvalas, A., Udvary, "Optical Wireless Communications: An Emerging Technology", Switzerland, Springer, 2016.

[3] Leitgeb, E., Plank, T., Awan, M.S., Brandl, P., Popoola, W., Ghassemlooy, Z., Ozek, F., Wittig, M., "Analysis and Evaluation of Optimum Wavelengths for Free-Space Optical Transceivers", in proccedings of 12th International Conference on Transparent Optical Networks (ICTON), Munich, Germany, 2010. pp. 1-7

[4] Leitgeb, E., Bregenzer, J., Gebhart, M., Fasser, P., Merdonig, A., "Free Space Optics – Broadband Wireless Supplement to FiberNetworks", in proccedings of SPIE, Free-Space Laser Communication Technologies XV, vol. 4975, San Jose, CA, 2003. pp. 57-68.

[5] Leitgeb, E., Gebhart M., Sheikh Muhammad, S., Flecker, B., Chlestil, C., "Measurement of Light attenuation in dense fog conditions for FSO applications", in proccedings of SPIE, Atmospheric Optical Modeling, Measurement, and Simulation, vol. 5891, Bellingham, WA, 2005. pp. 1-12.

[6] Leitgeb, E., Sheikh Muhammad, S., Flecker, B., Chlestil, C., Gebhart, M., Javornik, T., "The Influence of Dense Fog on Optical Wireless Systems, Analysed by Measurements in Graz for Improving the Link-Reliability", in proccedings of 8th International Conference on Transparent Optical Networks (ICTON), Nottingham, United Kingdom, 2006. pp. 154-159.

[7] Leitgeb, E., Birnbacher, U., Kogler, W., Schrotter, P., "High Availability of Hybrid Wireless Networks", in proccedings of SPIE, Reliability of Optical Fiber Components, Devices, Systems, and Networks II, vol. 5465, Bellingham, WA, 2004. pp. 238-249.

[8] Nur Islam, Nur Al Safa Bhuiyan. Effect of operating wavelengths and different weather conditions on performance of point-to-point free space optical link. International Journal of Computer Networks & Communications (IJCNC) Vol.8, No.2, March 2016

[9] Aderemi A. Atayero, Oleg I. Sheluhin and Yury A. Ivanov. Modeling, Simulation and Analysis of Video Streaming Errors in Wireless Wideband Access Networks. Springer. 2013.

PHASE NOISE OF THE EFFECTIVE LOCAL OSCILLATOR WAVEFORM IN HARMONIC REJECTION MIXERS

Ludwig Lubich

Technical University of Sofia, Faculty of Telecommunications
1000 Sofia, 8 Kl. Ohridski Blvd

lvl@tu-sofia.bg

Abstract

In this paper the relationship between the phase noise of the effective local oscillator waveform (ELOW) of harmonic rejection mixers (HRMs) and the phase noise of their clock oscillators is investigated. HRMs and conventional mixers are compared with respect to the phase noise level of their ELOWs. It was found that HRMs and conventional mixers have nearly equal phase noise levels especially at low frequency offsets.

1. INTRODUCTION

The noise sources in the oscillator circuits cause short-term, random fluctuations in the amplitude and the phase of the generated waveforms. They are known as amplitude and phase noise respectively. However, practical oscillators have some inherent amplitude-limiting mechanism, which strongly suppresses the amplitude noise. Therefore, the phase noise (PN) is the dominating one [1]. The PN can be seen as a phase modulation of the generated waveform and therefore, produces corresponding noise sidebands.

The oscillator PN causes harmful effects in wireless communications, such as reciprocal mixing, caused by the local oscillator PN in receivers [2] and interference in neighboring channels caused by the transmitter PN sidebands [2]. Therefore, the PN level is among the most important characteristics of RF oscillators. Usually the PN level is characterized by the power spectral density (PSD) of the noise sidebands at a particular offset from the oscillation frequency, related to the carrier level and is measured in dBc/Hz.

In the last decade, harmonic rejection mixers (HRMs) have gained in popularity because they greatly relax preselect filtering requirements in wireless receivers. An HRM is a complex mixer, consisting of several parallelly operating elementary hard-switching mixers, driven by respective rectangular pulse trains, derived from a common clock oscillator [3]. An HRM can be seen as a single multiplier, multiplying the input RF signal by an *effective* local oscillator waveform (ELOW) from which some harmonics are excluded. Obviously, the ELOW has its own PN, caused by the clock oscillator PN and other noise sources in the HRM circuit. Numerous publications on HRMs appeared, but to the best our knowledge, the phase noise of the HRM ELOW has not yet been investigated.

In this paper the phase noise transfer mechanism from the clock oscillator to the ELOW is examined and the relationship between the corresponding PN PSDs is expressed. The PN contribution of the rest of the HRM circuit will be subject of further research.

Next, it is useful to compare HRMs with conventional mixers (CMs), i. e. mixers not having harmonic rejection with respect to PN. Nowadays most of the CMs are hard-switching [2]. Due to abrupt switching, the actual local oscillator waveform (which is nearly sinusoidal) and the waveform, which effectively multiplies the input RF signal, are different. Therefore, it is suitable to use the term ELOW for CMs also. The PN level of the HRM ELOW should be compared with the PN level of CM ELOW and not with the PN level of its local oscillator itself.

The rest of the paper is organized as follows: In the next section, some preparatory considerations regarding phase noise are made. In Sections 3 and 4, the phase noise transfer from the clock oscillator to the ELOW of HRMs and conventional mixers, is examined, respectively. The phase noise PSDs of the ELOWs are derived in Section 5 and HRMs are compared with CMs with respect to PN level.

2. PHASE NOISE OF NON-SINUSOIDAL WAVEFORMS

ELOWs are non-sinusoidal; therefore it is important to specify what we understand by PN of a non-sinusoidal waveform.

A sinusoidal oscillation with PN can be expressed as $s(t)=A\sin[2\pi f_0 t+\phi(t)]$, where $\phi(t)$ represents the PN. (It happened to be more convenient to use sine instead of the widely accepted cosine.) Taking into account that $\phi(t)$ is small, we obtain:

$$s(t)\approx A[\sin(2\pi f_0 t)+\phi(t)\cos(2\pi f_0 t)]. \quad (1)$$

Let us consider a periodic non-sinusoidal noiseless waveform expressed by:

$$\bar{s}(t)= A\sin(2\pi f_0 t)+C_0 + \sum_{n=2}^{\infty}\dot{C}_n\cos(2\pi n f_0 t) \quad (2)$$

where the fundamental is the component of interest. If the corresponding noisy waveform can be expressed as

$$s(t)=\bar{s}(t)+A\phi(t)\cos(2\pi f_0 t), \quad (3)$$

then $\phi(t)$ can be interpreted as phase noise of $s(t)$.

3. HRM PHASE NOISE DERIVATION

There are numerous HRM implementation alternatives. To be specific we will examine a passive current commutating HRM as in [3], but the results will be applicable for most HRMs. The conceptual diagram of the HRM is given in Fig. 1, which is self-explanatory.

The ELOW can be easily found if a DC voltage of 1 V is imaginarily applied to the RF input. Then the ELOW will appear at the output. The ELOW is by nature a sinusoid uniformly sampled at a rate of Nf_{LO}, where N is the number of commutations per LO cycle. Therefore, ELOW contains nonzero harmonics only at frequencies of $kNf_{LO}\pm 1$, where $k=1,2,\ldots$.

In practical implementations, in order to avoid large voltage swings at the transconductance amplifier (TCA) outputs, they should be switched to ground (GND) in the time intervals when they are not connected to the transimpedance amplifier (TIA) input.

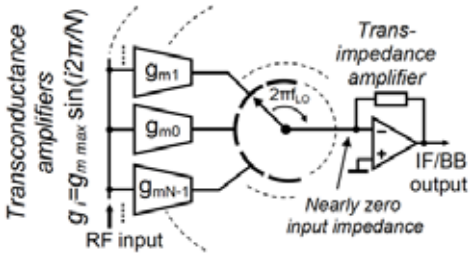

Figure 1. HRM operation principle

However, it is more rational to use the currently unneeded TCAs to form additional IF/baseband (BB) outputs. This makes possible the use of techniques for improved harmonic rejection, as in [3].

Naturally, the rotary switch is implemented by separate transistor switches. They are controlled by respective pulse trains V_{Ci}, derived by logic circuits from a clock oscillator (CO) running at $f_{CLK}=Nf_{LO}$.

The following assumptions were adopted:

1. MOS field-effect transistors (FETs) are used as switches. They operate in the deep triode region and their drain-source conductance is:

$g_{SW}=\beta(V_{DC}+V_G)$, where β is a MOSFET parameter, V_{DC} incorporates the FET threshold voltage and bias voltages, and V_G is the control voltage applied to the gate.

2. The duration t_{COM} of a commutation is at least an order of magnitude shorter than the clock period $T_{CLK}=1/f_{CLK}$.

3. The phase disturbance $\phi(t)$ of the CO in nearly constant in time intervals $\Delta t\le\phi(t)/(2\pi f_{CLK})$

4. The time shifts $\tau=\phi(t)/(2\pi f_{CLK})$ are orders of magnitude shorter than the commutation interval.

5. Without loss of generality, a TIA gain $G_{TIA}=1$ V/A and maximum a TCA transconductance $g_{m\max}=1$ A/V can be assumed.

6. The edge forming of the pulses controlling the switches can be adequately modeled by passing of the clock oscillator sine wave via limiting amplifiers with unsaturated voltage gain G_V.

In the ideal case, taking into account Assumption 5, ELOW can be easily expressed as:

$$LO_{eff}(t)=v_{out}(t)/v_{RF}(t) = \sum_{i=-\infty}^{\infty}\sin\left(i\frac{2\pi}{N}\right)\mathrm{rect}\left(\frac{t-iT_{CLK}}{T_{CLK}}\right). \quad (4)$$

It can be established that the first harmonic amplitude of ELOW is $(N/\pi)\sin(\pi/N)$.

The clock oscillator phase noise can affect the ELOW only during the commutations. Outside the commutation intervals, the TCA outputs are firmly connected to the TIA inputs. This can be modeled by multiplying the phase noise by corresponding time shifted pulses $p(t)$ with unity amplitude and duration t_{COM}.

The clock oscillator waveform is given by

$$v_{OSC} = \sin(2\pi f_{CLK} t) + \phi_{OSC}(t)\cos(2\pi f_{CLK} t) \quad (5)$$

where $\phi_{OSC}(t)$ represents the CO phase noise.

In order to have a zero initial phase of the ELOW fundamental, the commutations take place around the time instants $iT_{CLK} + T_{CLK}/2$ (Fig. 2). Taking into account Assumption 2, the following approximation of (5) can be used in the commutation intervals:

$$v_{OSC} \approx -2\pi f_{CLK}(t - iT_{CLK} - T_{CLK}/2) - \phi_{OSC}(t). \quad (6)$$

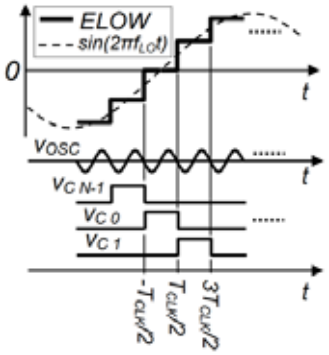

Figure 2. HRM timing

For the controlling pulses *in the commutation intervals* $v_{Ci} = \mp G_V v_{OSC}$ is fulfilled (Fig. 3). The sign alternates for rising and falling edges.

Let us consider the commutation of the j^{th} TIA input from the i^{th} to the $i+1^{st}$ TCA output. The corresponding HRM fragment with the four switches involved is given in Fig. 4. The switch conductances $g_{i,j+1}$ and $g_{i+1,j}$ increase from zero to their "on" values, and $g_{i,j}$ and $g_{i+1,j-1}$ decrease from their "on" values to zero. The commutation begins just when the conductance of the two initially open switches is no longer zero and ends when the conductance of the two initially closed switches becomes zero.

In the commutation intervals, V_C changes from $-V_{DC}/2$ to $V_{DC}/2$ for the closing switches and from $V_{DC}/2$ to $-V_{DC}/2$ for the opening switches, as can be deduced taking into account Assumption 1 (Fig. 3).

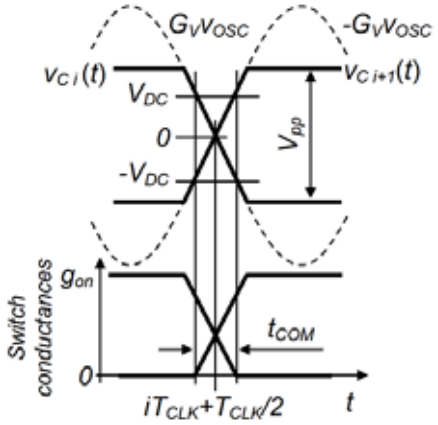

Figure 3. Switch conductances in the i-th commutation

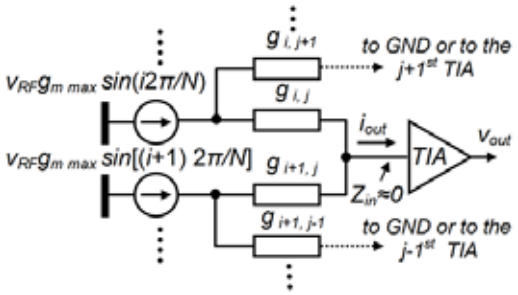

Figure 4. Commutation from the i-th to the i+1-st TCA output

For the considered commutation can be written:

$$\frac{i_{out}}{v_{RF}} = \sin\left(i\frac{2\pi}{N}\right)\frac{g_{SW\,i,j}}{g_{SW\,i,j} + g_{SW\,i,j+1}} + \sin\left[(i+1)\frac{2\pi}{N}\right]\frac{g_{SW\,i+1,j}}{g_{SW\,i+1,j} + g_{SW\,i+1,j-1}} \quad (7)$$

Taking into account Assumption 5, we have $i_{out} = v_{out}/G_{TIA} = v_{out}$; therefore, (7) gives indeed v_{out}/v_{RF}, which is $LO_{eff}(t)$. Substituting in (7) the switch conductances according to Assumption 1, we obtain:

$$LO_{eff}(t) = \sin\left(i\frac{2\pi}{N}\right)\left(\frac{1}{2} + \frac{G_V v_{OSC}}{2V_{DC}}\right) + \sin\left[(i+1)\frac{2\pi}{N}\right]\left(\frac{1}{2} - \frac{G_V v_{OSC}}{2V_{DC}}\right) \quad (8)$$

After substituting of v_{OSC} in (8) and rearranging, we separate only the noise component $n_i(t)$ for the i^{th} commutation. We obtain the total ELOW noise $n(t)$ by summing all $n_i(t)$, multiplied by the corresponding pulses:

$$n(t) \approx \frac{G_V}{V_{DC}} \sin\left(\frac{\pi}{N}\right) \cos(2\pi f_{LO} t) \times \phi_{OSC}(t) \sum_{i=-\infty}^{\infty} p\left[t - \left(\frac{T_{CLK}}{2} + iT_{CLK}\right)\right] \quad (9)$$

After inspecting (9) and comparing it with the noise term in (3), we can recognize that the noise of ELOW is only a phase noise and it is the phase noise of the clock oscillator, non-ideally sampled at rate f_{CLK} and scaled by magnitude.

To obtain the ELOW phase noise $\phi_{ELOW}(t)$, (9) should be expressed in the form $n(t) = A\cos(2\pi f_{LO} t)\phi_{ELOW}(t)$, were $A = (N/\pi)\sin(\pi/N)$ is the fundamental amplitude of the ELOW. After multiplying and dividing (9) by (N/π), and realizing that $V_{DC} = G_V 2\pi f_{CLK} t_{COM}/2$, we obtain:

$$\phi_{ELOW}(t) \approx \frac{1}{N}\frac{T_{CLK}}{t_{COM}} \times \phi_{OSC}(t) \sum_{i=-\infty}^{\infty} p\left[t - \frac{T_{CLK}}{2} - iT_{CLK}\right] \quad (10)$$

Eq. (10) was verified by Matlab simulations.

A similar expression for $\phi_{ELOW}(t)$ was also derived after replacing Assumption 6 with the following assumption: The switching of the logic gates producing the control pulses is extremely abrupt and the CO PN affects the ELOW instantaneously only at its zero-crossing instants, shifting the ELOW transitions by $\phi(iT_{CLK} + T_{CLK}/2)/\omega_{CLK}$. In this case, the PSD of ϕ_{ELOW} for the frequencies of interest was the same as the PSD obtained here.

4. CONVENTIONAL MIXER PN

The equivalent circuit diagram of a conventional current commutating double balanced mixer is given in Fig. 5. Note that usually two commutations take place in one cycle of the local oscillator.

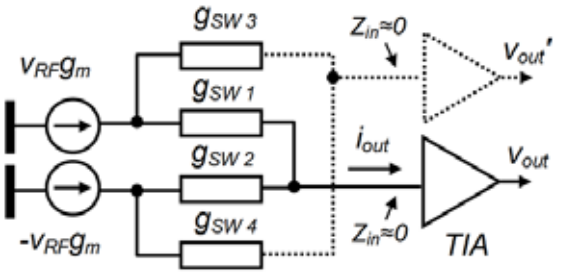

Figure 5. Equivalent circuit of a CM

Without loss of generality we assume $g_m = 1$ and $G_{TIA} = 1$. In a similar way as in the previous section we obtain for the ELOW in the commutation interval:

$$LO_{eff} = \frac{g_{SW1}}{g_{SW1} + g_{SW3}} - \frac{g_{SW2}}{g_{SW2} + g_{SW,4}} = \frac{G_V v_{OSC}}{V_{DC}}. \quad (11)$$

The noise in the ELOW is:

$$n(t) = \frac{G_V}{V_{DC}} \cos(2\pi f_{LO} t) \times \phi_{OSC}(t) \sum_{i=-\infty}^{\infty} p\left(t - i\frac{T_{LO}}{2}\right). \quad (12)$$

Taking into account that the amplitude of the first harmonic of the ELOW is $4/\pi$, we express (12) in the following form:

$$n(t) = \frac{4}{\pi} \cos(2\pi f_{LO} t)\phi_{ELOW}(t), \quad (13)$$

where

$$\phi_{ELOW}(t) = \frac{T_{LO}}{4t_p}\phi_{OSC}(t) \sum_{i=-\infty}^{\infty} p\left(t - i\frac{T_{LO}}{2}\right) \quad (14)$$

represents the phase noise of the CM ELOW It is the PN of the actual local oscillator, non-ideally sampled at rate $2f_{LO}$ and scaled by magnitude.

5. PHASE NOISE PSD

The PN PSD is found as

$$S_{HRM}(f) = \lim_{T\to\infty} \frac{\mathrm{E}\left[\left|\dot{\Phi}_{ELOW}(f)_T\right|^2\right]}{T} \quad (15)$$

where $\dot{\Phi}_{ELOW}(f)_T$ is the Fourier transform of $\phi_{ELOW}(t)$; the subscript T and $\mathrm{E}[X]$ denote a truncation to a finite time interval T and expectation, respectively [4].

$$\dot{\Phi}_{ELOW}(f)_T = \\ = \frac{1}{Nt_{COM}} \sum_{i=-\infty}^{\infty} \dot{P}(iNf_{LO}) \dot{\Phi}_{OSC}(f - iNf_{LO})_T \quad , \quad (16)$$

where $\dot{P}(f)$ and $\dot{\Phi}_{OSC}(f)_T$ are the Fourier transforms of $p(t)$ and $\phi_{OSC}(t)$, respectively. Strictly speaking, the CO PN is correlated in frequency domain, but this can be neglected in most cases. Then for the PN PSD, we obtain:

$$S_{HRM} = \left(\frac{1}{Nt_{COM}}\right)^2 \\ \times \sum_i P(iNf_{LO})^2 S_{OSC}(f - if_{CLK}) \quad , \quad (17)$$

where S_{OSC} denotes the PN PSD of the CO and $P(f) = |\dot{P}(f)|$.

For a given ELOW frequency, an HRM requires an oscillator whose frequency is N times higher than that one required by a conventional mixer. Under equal other conditions, the PN PSD of an oscillator running at an N times higher frequency, is expected to be nearly N^2 times higher, as can be deduced from [1]. Therefore, in order to make a fair comparison between HRMs and conventional mixers, we choose $S_{OSC} = N^2 S_{LO}$, where S_{LO} is the PN PSD of the conventional mixer local oscillator. Then

$$S_{HRM} = (1/t_{COM})^2 \\ \times \sum_i P^2(iNf_{LO}) S_{LO}(f - iNf_{LO}) \quad . \quad (18)$$

In a similar way, we obtain the PN PSD of the conventional mixer as:

$$S_{CM} = (1/4)(1/t_{COM})^2 \\ \times \sum_i P^2(i2f_{LO}) S_{LO}(f - i2f_{LO}) \quad (19)$$

In both cases, the PN PSD is a sum of scaled frequency shifted replicas of the oscillator PN PSD. In typical cases, the PN PSD of oscillators falls rapidly with the frequency offset, so the close-in PN PSD of the ELOW will be a scaled replica of the oscillator PN PSD. Then it can be seen that S_{HRM} is 4 times higher than S_{CM}.

At this point, work is almost done, but we need to know the PSD of the sidebands caused by PN rather than the PN PSD itself. It is commonly assumed that the PSD of the noise sidebands are a frequency translated and scaled by $1/4$ replica of the PN PSD. This is an acceptable approximation if the PN PSD is low enough at $f \geq f_0$. However, this is not the case when the PN is sampled. Indeed, the multiplication of the PN by the cosine (see Eq. 3) produces a sum of two PN spectrum replicas, shifted by $\pm f_{LO}$, or shifted by $2f_{LO}$ to each other. Since the PN in conventional mixers has a sampling rate of $2f_{LO}$, the PN spectrum has a periodicity of $2f_{LO}$. Therefore, the summation results in a doubled noise voltage or the resultant PSD becomes 4 times higher. In contrast, in HRMs the PN sampling frequency is Nf_{LO}, and the frequency shift by $2f_{LO}$ leads to summation of uncorrelated components. Therefore, the resultant PSD is a sum of two shifted replicas of S_{HRM}. In addition, for small offset frequencies, in practical cases, the PDS replica, which is shifted by $+f_{LO}$, dominates and practically fully determines the resultant PSD. Hence, the PN levels of HRMs and CMs are the same at relatively low frequency offsets. This statement was verified by Matlab simulations.

6. CONCLUSION

In general, the level of the PN transferred from the CO to HRM ELOWs is the same as in CMs. In contrary to some intuitive guesses, the CO PN causes only PN in HRM ELOW (and not amplitude noise or/and harmonic suppression degradation). The investigations confirmed the expectation that the ELOW PN is by nature sampled at a rate of f_{CLK} clock oscillator PN.

Further research should be done to evaluate the PN contribution of the rest of the HRM circuit. This, along with the results presented here, will allow us to decide conclusively whether the use of HRMs instead of CMs in wireless devices is at the expense of phase noise performance degradation.

References

[1] T. H. Lee, A. Hajimiri, "Oscillator Phase Noise: A Tutorial", IEEE Journal of Solid-State Circuits, Vol. 35, No. 3, March 2000, pp. 326-336.

[2] B. Razavi, RF Microelectronics, Prentice Hall PTR, 2011

[3] Z. Ru et al., "Digitally-Enhanced Software-Defined Radio Receiver Robust to Out-of-Band Interference", IEEE Journal of Solid-State Circuits, Vol. 44, No 12, Dec. 2009, pp. 3359-3375.

[4] D. Vasilyev et al., Radiotechnical circuits and signals, Radio i svyaz, 1982 [In Russian].

FREQUENCY DOMAIN ANALYSIS OF BIOMEDICAL SIGNALS

Viktor A. Nedialkov

Technical University - Sofia, Faculty of Telecommunication,
8, "Kliment Ohridsky" str., 1000 Sofia, Bulgaria

Abstract

The paper illustrates signal processing techniques used in the analysis of biomedical signals such as EMG, EEG and Heart Rate Variability, in the frequency domain. Normalization of the signals, FFT transform, windowing and quantitative variable calculations are demonstrated. Using modern programming languages new algorithm are developed for each part of the analysis. The result of this study is a synthesized toolset with algorithms and equations ready to be used in various biomedical signal frequency domain analisys.

1. INTRODUCTION

Frequency domain analysis is very important in the biomedical signal processing. With the rapid improvement of the processing power it is becoming much more usable in various signal analysis even in real time signal processing.

In order to produce the expected results the signal transformations must be performed in very specific sequence and the transformations themselves must be performed accurately.

The most common biomedical signal analysis to date are of the Heart Rate Variability (HRV) for calculating parameters describing the low frequency changes in the HR. This parameters are useful for predicting the risk of developing myocardial infarction and sudden cardiac death. Other area of Frequency analysis is the EEG (Electroencephalogram) where calculating the power spectrum of the signals correlate to the function of specific brain functions and are very important for the brain diagnostics. EMG is another area of use of the frequency domain analysis. The calculated spectrum density shows how much each frequency contribute to the muscle contraction, which can be very useful for neurological and muscle disorders. This type of analysis combined with time domain algorithms can improve significantly the reliability of an EMG driven active prosthesis.

In the bottom of every frequency domain analysis lays the Discrete Furrier Trasnform (DFT) and its computational version Fast Furrier Transform (FFT).

But you can't just put a time series into an FFT and get a frequency domain data. There are many signal and algorithm specific procedures to make in order to have an accurate and predictable results. This includes: interpolation – not all biomedical time series are uniformly discretizated signals. Windowing: this is to minimize the effect of spectral spread due to the DFT expecting the input sequence to be periodic. Then we have the DFT itself in the form of FFT algorithm. Then we have to normalize the result of the FFT which is a complex vector, into a real value representing the frequency spectrum. And at last we may need to average the result of several transformations to reduce the variance error.

All these transformations are described in the following sections.

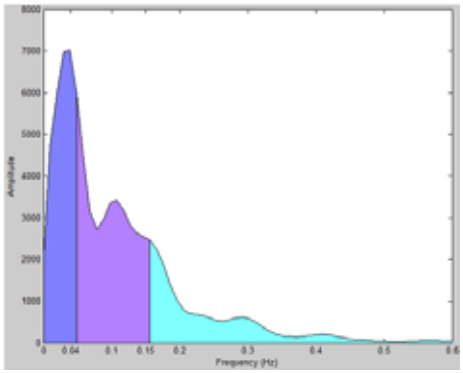

Fig. 1. HRV PSD Distribution

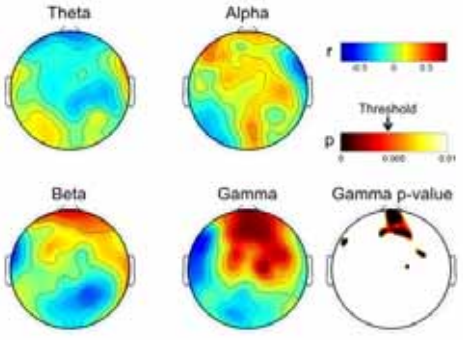

Fig. 2. EEG Frequency mapping

2. INTERPOLATION OF THE SIGNAL

Not all biomedical signals are uniformly sampled series. For example an RR interval time series is a series representing the intervals between two adjacent QRS complexes. In order to obtain a uniform sample frequency we need to resample or interpolate the time series.

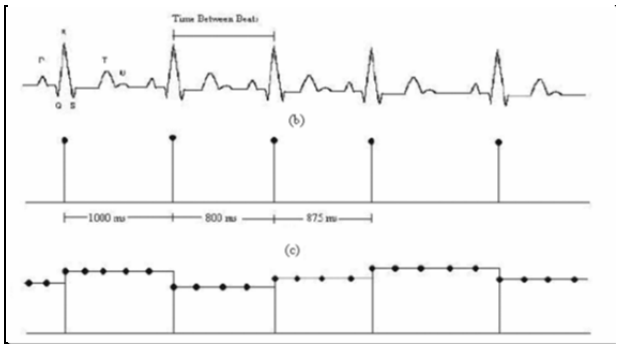

Fig. 3. Interpolation of the RR interval time series

There are two main methods for interpolation used – Linear interpolation and Cubic spline interpolation. The first one is more straight-forward and is suitable for signals which are not with sinusoidal origin and the cubic spline interpolate more accurate the sinusoidal signals.

Resampling is needed also when we need higher bandwidth analysis then the actual sampling frequency in order to meet the Nyqust criteria.

3. WINDOWING

If we simply take a stretch of length N out of a time series containing a sinusoidal signal and perform a DFT, we will most likely _nd that the sinusoidal signal which we might naively expect to result in a sharp peak in only one frequency bin, will instead show up as something ugly like shown in Figure 4. The reason is that the DFT implicitly assumes that the signal is periodic, i.e. that the time series of length N repeats itself in_nitely in a cyclic manner. If the frequency of the sinusoidal input signal is not an exact multiple of the frequency resolution fres, i.e. does not fall in the exact center of a frequency bin, this assumption is not true, and the DFT will `see' a discontinuity between the last sample and the _rst sample due to the cyclic continuation. That discontinuity spreads power all across the spectrum.

The remedy is to multiply the time series with a 'window function' in the time domain before applying the DFT. This window function starts near or at zero, then increases to a maximum at the center of the time series and decreases again. Thus the discontinuity is removed. Many window functions have been defined and given names. They usually involve some compromise between the width of the resulting peak in the frequency domain, the amplitude accuracy and the rate of decrease of the spectral leakage into other frequency bins.

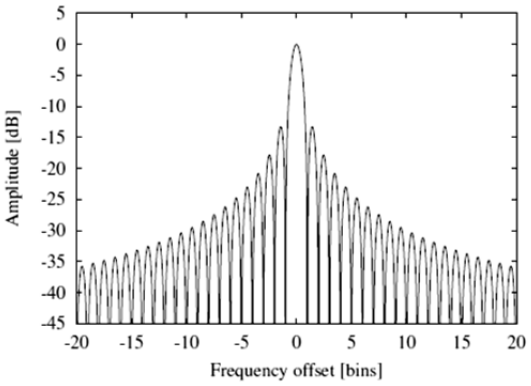

Fig. 4. Frequency response to a rectangular window

For our purpose we are using the simple but useful Hanning window.

A window function to be used with a DFT of length N is defined by a vector of real numbers {wj}, j = 0 ... N -1. It is used by multiplying the time series xj with the window before performing the DFT, i.e. using x1j = xj *wj as input to the DFT.

The Hanning window is defined as follows:

$$w_j = \frac{1}{2}\left[1 - \cos\left(\frac{2\pi.j}{N}\right)\right] \; ; \; j = 0 \ldots N-1,$$

We define the following two sums for normalization purposes:

$$S_1 = \sum_{j=0}^{N-1} w_j \, ,$$

$$S_2 = \sum_{j=0}^{N-1} w_j^2 \, .$$

We will use them in the normalization of the complex result of the DFT.

Because we will use S1 and S2 in the normalization of our final results, we can multiply the window values wj with any convenient constant factor.

4. FFT

After we have calculated the windowed time sequence we are ready to compute the DFT with the FFT algorithm. We are using a Radix2 FFT in our study.

We have developed a function

Radix2(XREtmp, XIMtmp, Nf);

It takes as parameters the data arrays for the real and imaginary part of the result and the length of the time series.

The code of the Radix2 implementation is not shown here but it is a classic Radix2 algorithm shown in many articles around the internet.

4. SCALING AND NORMALIZATION

The normalized equivalent noise bandwidth NENBW of the window, expressed in frequency bins, is given by

$$\mathrm{NENBW} = N\frac{S_2}{(S_1)^2}.$$

The effective noise bandwidth ENBW is given by

$$\mathrm{ENBW} = \mathrm{NENBW}.f_{\mathrm{res}} = \mathrm{NENBW}.\frac{f_s}{N} = f_s\frac{S_2}{(S_1)^2},$$

where f_S is the sampling frequency and f_{res} the width of one frequency bin. For the Hanning window we have NENBW = 1:5 bins. This equivalent noise bandwidth is required when the resulting spectrum is to be expressed as spectral density (such as for noise measurements). It can be understood by considering white noise as input to our algorithm. Due to the width of the window in the frequency domain, each frequency bin collects not only the noise in that frequency bin, but also from adjacent bins. Dividing the result by the effective noise bandwidth corrects for this phenomenon.

Now we come back to the problem of normalizing the results of the FFT. Assume we have an input time series x_j of length N. After multiplication with the chosen window function, it is subjected to a real-to-complex FFT as defined in the previous section. We will also need the window sums S1 and S2 defined in section 3.

The result of the FFT is a complex vector y_m of length N = 2 + 1. We interpret it as a power spectrum, expressed as $V^2{}_{\mathrm{rms}}$, as follows:

$$PS_{\mathrm{rms}}(f_m = m.f_{\mathrm{res}}) = \frac{2|y_m|^2}{S_1^2};$$

$$m = 0 \ldots N/2,$$

The factor S1 takes the role of N. It takes into account both the length N of the DFT and the gain of the window function, plus any constant factor that was used in the computation of the window values w_j.

The factor 2 originates from the fact that we use an effcient FFT algorithm that does not compute the redundant results for negative frequencies.

We now return to the scaling of the "normal" results. If the desired result is a power spectral density (PSD) expressed in V^2/Hz, it is obtained by dividing the power spectrum (PS) by the effective noise-equivalent bandwidth ENBW:

$$\mathrm{PSD}_{\mathrm{rms}}(f_m = m.f_{\mathrm{res}}) =$$

$$= \frac{\mathrm{PS}_{\mathrm{rms}}(f_m)}{\mathrm{ENBW}} = \frac{2|y_m|^2}{f_s.S_2}; \quad m = 0 \ldots N/2,$$

Since the ratio between the peak and the noise plateau in the FFT output depends on N, we need to distinguish carefully between spectra and spectral densities. The magic number to convert them into each other is the effective noise bandwidth ENBW, which should hence always be recorded when a spectrum or spectral density is computed, such that the result can be converted to the other form at a later stage, when the information about the frequency resolution f_{res} and the window that was used is normally not easily available any more.

Further processing of the output is straightforward: If the desired result is a linear spectrum (expressed in V) or a linear spectral density (expressed in V/pHz), simply take the square root of the corresponding power spectrum or spectral density:

$$\mathrm{LSD} = \sqrt{\mathrm{PSD}},$$

$$\mathrm{LS} = \sqrt{\mathrm{PS}}.$$

Finally the result can be converted into other units (such as Vpk or dB).

5. AVERAGING AND OVERLAP

If we compute one estimate of a spectrum with the methods described so far (i.e. multiplying one segment of the time series with a suitable window function, performing a DFT and scaling the results), we will typically find the result to be rather `noisy'. The theory confirms this practical observation: The standard deviation of the spectrum estimate in one frequency bin is equal to the estimate itself, i.e. 100%, if the signal in that bin is stochastic. It does not help the increase the length N of the DFT; that only reduces the width of one frequency bin without improving the variance.

The usual remedy is to take the average of M estimates and hence reduce the standard deviation of the averaged result by a factor of $1=\sqrt{M}$. However, the properties of the signal must remain stationary during the averaging. Note that the averaging must be done with the power spectrum (PS) or the power spectral density (PSD), not with their square roots LS or LSD. If the square roots are desired as result, they must be computed at the end after the averaging is finished. In conjunction with the use of window functions, this method of averaging several spectra is also known under names such as "Welch's method of averaging modified periodogramms", "Welch's overlapped Segmented average" etc.

If a long continuous data stream is simply split into several non-overlapping segments of length N and each segment is processed by a DFT with a window function, we have a situation as illustrated in Figure 5.

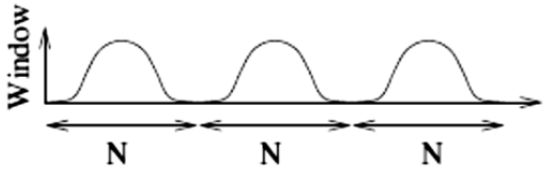

Fig. 5. Segmented data stream with window and without overlap

Due to the fact that the window function is typically very small or zero near its boundaries, a significant portion of the data stream is effectively ignored in the analysis. This is clearly not optimal in those situations where the data stream was produced at great expense, and maximal possible information is to be extracted from it. The situation can be improved by letting the segments overlap, as illustrated in Figure 6.

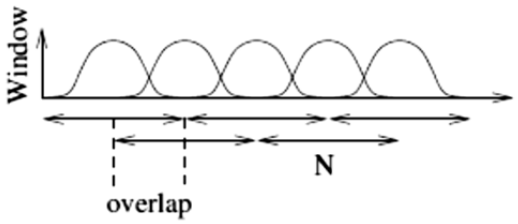

Fig. 6. Segmented data stream with windows and overlap

Figure 7 and Figure 8 shows the PSD calculated from a single and multible averaged data segments. The averaged result is much smoother.

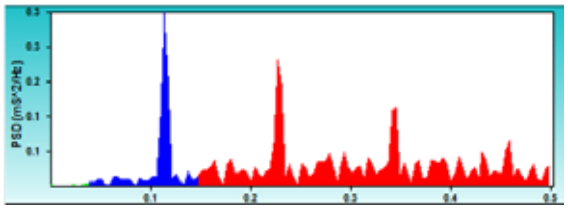

Fig. 7. Power spectrum density form a single data segment

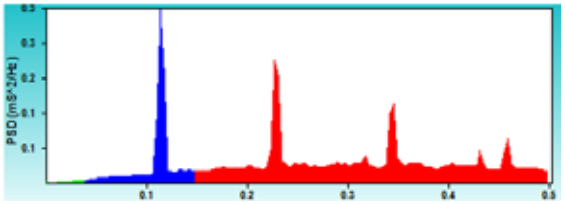

Fig. 8. Power spectrum density from several averaged data segments

6. CONCLUSIONS

The transformation of the signals from the time domain to the frequency domain must be performed very carefully and all of the above procedures must be performed in order to produce accurate results. Further studied must be performed on the different windows that can be used with the DFT. Also we did not remove the constant component of the signal which will appear in the bin 0 in the transformed signal.

Understanding the exact procedures for transforming time series into frequency domain gives us invaluable instrument for analysis of biomedical signals and effectively develop new algorithms for all kind of biomedical devices.

References

[1] Rangaraj M. Rangayyan "Biomedical Signal Analysis" Wiley-Interscience.

[2] Webster J, "Medical Instrumentation – application and design" John Wiley & Son.

[3] R. Ivanov, "Digital processing of single dimensional signals", Almamater international.

[4] G. Nenov, "Signals and systems", Novi Znania.

[5] R. Ivanov, "Digital processing of single dimensional signals", Almamater international

[6] G. Heinzel, A. Ruudiger and R. Schilling "Spectrum and spectral density estimation by the Discrete Fourier transform (DFT), including a comprehensive list of window functions and some new at-top windows", Max-Planck-Institut fur Gravitationsphysik

[7] Andrew J. Barbour and Robert L. Parker, "Normalization of Power Spectral Density estimates"

[8] J. Schesser "HRV Analysis" BME 333 Biomedical Signals and Systems.

MULTIFUNCTIONAL SYSTEM FOR PHYSIOTHERAPY

Atanas Dimitrov*, Sasho Guergov**, Dimiter Tz. Dimitrov*

Faculty of Telecommunication*, Faculty of Industrial Technology**,
Technical University - Sofia,8, "Kliment Ohridsky" str., 1000 Sofia,Bulgaria,

Abstract

An investigation on structure of one multifunctional adaptive system for physiotherapy with measurement devices has been done in the paper. In the paper there are descriptions of different parts of the multifunctional system. Some characteristics and properties of different units of multifunctional system have been done, also. Some possibilities for simultaneously applications of different system's units are described, also. It's important to provide simultaneously application of different system's units only when their physiological influences on the human body are compatible. Simultaneously application of magneto-therapy, mechanical acupressure and cranial electro stimulation are described in the paper.

1. INTRODUCTION

There are many well know methods for physiotherapy, which can be applied in different cases of pathology. Often according to these methods there is a separate "hard" application of different external influences one by one. One new tendency in medicine is connected with application of multifunctional adaptive systems for physiotherapy. These systems can provide not only separate influence of different external influences, but simultaneously influence of these external influences of on one or on different part of the human body. Some times a physical interaction between these external influences can be seen as in the case of simultaneously influence of low frequency electrical and magnetic fields. In other cases there is not formal physical interaction between external influences, but there is physiological interaction as in the cases of simultaneously influence of low frequency magnetic field and acupressure or acupressure and Cranial Electrotherapy Stimulation (CES). CES is the application of low-level pulsed electrical currents (usually less than 1mA) applied to the head for medical and/or psychological purposes. It would be very convenient for physicians if much more units for different external influences would be available as parts of one multifunctional adaptive system for physiotherapy. For instance this system can provide influence of low frequency magnetic field, low frequency electrical field (including Cranial Electrotherapy Stimulation) and acupressure.

2. DESIGN OF DEVICES FOR CREATING OF LOW FREQUENCY MAGNETIC FIELD

The application of China's method for acupressure is very actual in medical therapy, now. Usually physician provide application of acupressure by his hands. It's inconvenient first of all for physician. He's able to work for short time. Then he can continue after relax, but the number of these procedures per day are limited. In other side it would be better to provide acupressure simultaneously on more points on the human body. It's impossible because physician has only two hands.

The results of therapy by acupressure would be more good if there would be provided more intensive movement of the blud in around the points of acupressure. This activation of blud's movement can be provided by application of low frequency magnetic field together with acupressure.

It's clear that it' s necessary to provide special device for acupressure, which can be used together with special device for creating of low frequency magnetic filed around the points for acupressure. Therefore the application of system for simultaneously application of acupressure and low frequency magnetic field is very actual, now.

Usually the low frequency magnetic field can be created using two coils, connected to the output of apparatus for magneto-therapy. This apparatus is a source of special electrical signals for the coils.

Often the application of above described method for therapy is on the hand because there are situated many points of acupunctures.

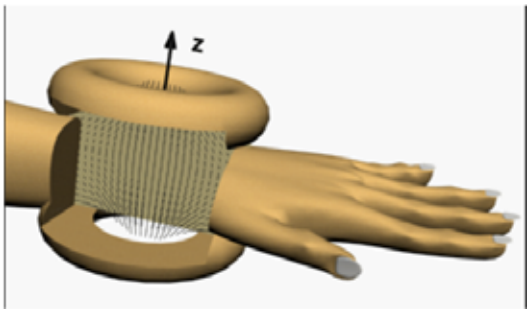

Fig. 1. A possibility for disposition of two coils on the hand

The space configuration of the lines of vector of magnetic induction can be seen on fig. 1.

It's well known that on the *spine* there are many points of acupuncture, also. Some examples for disposition of coils on the spine can be seen on fig. 2.

The axis of space components of magnetic induction of magnetic field, created by different coils can be seen on fig. 2, also.

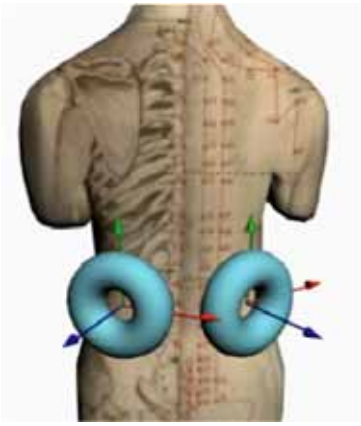

Fig. 2. Some examples for disposition of coils on the spine

A girdle coil (fig.3) can be used for magneto-therapy, also.

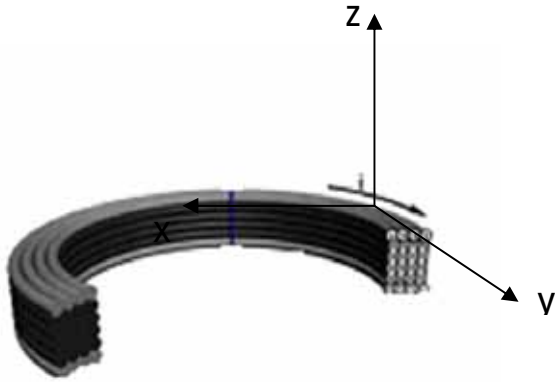

Fig. 3. A girdle coil

3. MEASUREMENT OF PARAMETERS OF LOW FREQUENCY MAGNETIC FIELD

First of all it's important to provide measurement of the value of magnetic induction in the process of magneto-therapy. The sensor has been putted in different points around the girdle coil. The measurement of the gidle coil's current has been done by ordinary ampermeter. The measurement of module of magnetic induction on the axes X and Z (Fig. 3) has been done. The results of experimental measurements together with the results of calculation of the module of magnetic induction on axis X can be seen on Fig. 4.

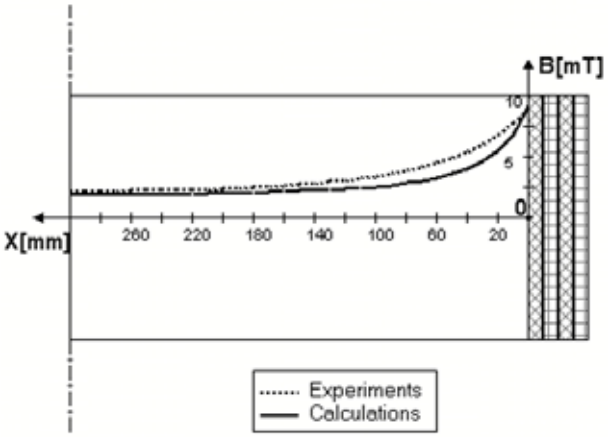

Fig. 4. Module of magnetic induction on the axis X

The results of experimental measurements together with the results of calculation of the module of magnetic induction on axis Z can be seen on Fig. 5.

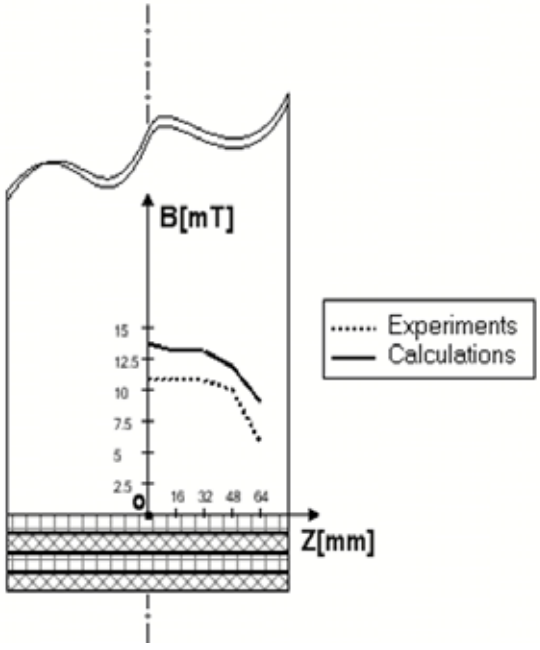

Fig. 5. Module of magnetic induction on the axis Z

4. LEVEL OF ERRORS OF MEASUREMENT OF THE VALUE OF MAGNETIC INDUCTION

The main causes for errors between calculated and measurement results are: the finite sizes of the sensor. The results of calculation and results of experimental measurements are similar. It was the main goal of investigation. Of course it's possible to obtain more precise methods and measurement devices, but it's not necessary in the case of magnetotherapy, where usually the values of magnetic induction are 10-30 mT and 10% error is acceptable. It's clear that only one small translation of the human body in the girdle coil would be enough for an error of the value of module of magnetic induction in an arbitrary point of the human body, more than 10%. The value of relative magnetic permeability of live tissue $\mu_r \approx 1$ as in the air.

Therefore computer simulation can be used successfully for future investigation of space configuration of low-frequency magnetic field in the human body, also. This is the main conclusion of the above investigations.

5. DESIGN OF DEVICES FOR CREATING OF CRANIAL ELECTROTHERAPY STIMULATION

Often, in the last time there is application of therapy by acupressure simultaneously with electrotherapy especially with Cranial Electrotherapy Stimulation. Usually physician provide application of acupressure by his hands and he should be very careful because this therapy is on head. Of course it's possible to be used separately one by one both therapy by acupressure and Cranial Electrotherapy Stimulation, but the effect of therapy especially effect of relaxation would be more good in the case of simultaneously application.

Sometimes in the cases of high values of the blood pressure, stress and loss of the sleep physicians use successfully a unit for magneto-therapy for decreasing of blood pressure and Cranial Electrotherapy Stimulation for sleeping using an other unit for electro-seeping. In the last time often physicians use both magneto-therapy and electro-sleeping simultaneously. This allow them to obtain more good effect of therapy. The method of Cranial Electrotherapy Stimulation is new one since the end of last century. Therefore some preliminary separate investigation of this method has been done before simultaneously application of the method together with magneto-therapy or/and acupressure.

CES treatment may result indirectly in increased blood flow to the brain. Hence its possible contra-indication in recent hemorrhagic stroke patients. This same effect can cause brief increased blood flow beneath the electrodes behind the ears. This redness should not be cause for concern. This is an extremely rare occurrence. Cranial electrotherapy stimulation devices are generally similar in size and appearance to standard transcutaneous electrical nerve stimulators (TENS), but produce very different waveforms. Standard milliampere-current TENS devices must never be applied transcranially. CES electrodes can be placed bitemporally, bilaterally in the hollow behind the ears just anterior to the mastoid processes, or clipped to the earlobes. This depends on the device being used. Most CES devices should produce a pulse repetition rate (PRR) of 100 Hz.Some produce a PRR as low as 0.5, or as high as 15,000 Hz. Most CES units are user friendly. After having put on either the electrodes or the ear-clips and inserted the lead wire into the jack, it's all very simple. CES units either feature an on-off knob that also controls the amplitude (turning it to the right increases the amount of current) as in the 100 Hz devices. A CES generates an adjustable current of 80 to 600 μA that flows through clips placed on the earlobes. The waveform of this device is a 400 milliseconds positive pulse followed by a negative one of the same duration, then a pause of 1.2 seconds. The main frequency is 0.5 Hz, i.e. a double pulse every 2 seconds. Current output is limited to 600 μA max and can be regulated from 80 to 600μA. A LED can flashes every 2 seconds signaling proper operation and can also be used for setting purposes.

A common CES configuration is 100 Hz with a maximum current output of 1.5 mA, current amplitude similar to that in the human body. A device of CES as part of multifunctional system for physiotherapy can be seen on fig. 6.

Fig. 6. Device for Cranial Electro Stimulation

6. DESIGN OF MECHANICAL DEVICE FOR ACUPRESSURE

The design of mechanical devices for acupressure should be connected with design of coils for magneto-therapy as the multifunctional system should provide simultaneously application of acupressure and magneto-therapy. It's well known that magnetic filed can increase the velocity of ions of blood. Because of that the effect of acupressure can be more good. Usually the line of mechanical pressure is the axis of coils. The sizes of coils can be different according to the sizes of "active" area around of the acupuncture points.

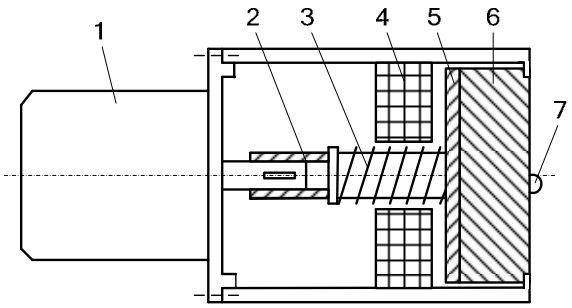

Fig. 7. Mechanical device for acupressure

On fig. 7 can be seen a mechanical device for acupressure, when:

1 – motor;
2 – axle;
3 – shaft;
4 – a coil, which provides axial movement of the shaft;
5 – metal disk;
6 – plastics body;
7 – massage pimple (osezatel).

The modified device for acupressure simultaneously with low frequency magnetic field can be seen on fig. 8. It can be seen that the shaft is in the coil for magnetotherapy.

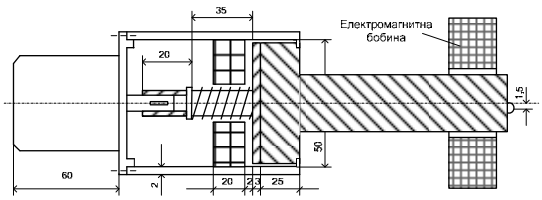

Fig. 8. Modified mechanical device for acupressure simultaneously with application of low frequency magnetic filed

7. CONCLUSION

1. It's clear that the process of physiotherapy can be more effective in the case of simultaneously application of several unites (apparatuses or/and devices) for different physical influences on the human body than separate application of these unites one by one.

2. The big advantage of one multifunctional system for physiotherapy is that it's flexible and user friendly. Therefore it's easy to be obtained different configuration of system and to provide applications of many methods for physiotherapy. Because of that the system is adaptive to medical methods for therapy.

3. Usually every multifunctional system can be developed easy. It's enough to add new units which should be compatible with the rest system's units.

The use of footnotes is discouraged. Include necessary secondary explanations in the text (within parentheses) if you need additional comments.

References

[1] Kirsch, D.L. and Smith, RB. The use of cranial electrotherapy stimulation in the management of chronic pain: A review. NeuroRehabilitation 14 (2000) p.85-94.

[2] Winick, R.L. Cranial electrotherapy stimulation (CES): a safe and effective low cost means of anxiety control in a dental practice. Gen. Dent. 47 (1999) p. 50-55.

[3] Lichtbroun, A.S., Raicer, M.C. and Smith R.B. The treatment of fibromyalgia with cranial electrotherapy stimulation. J. Clin. Rheumatol. 7 (2001) p.72-78.

[4] Hozumi, S, Hori, H, Okawa, M, Hishikawa, Y and Sato, K. Favorable effect of transcranial electrostimulation on behavior disorders in elderly patients with dementia: a double-blind study. Inter. J. Neurosci. 88 (1996) p.1-10.

[5] Southworth, S. A study of the effects of cranial electrical stimulation on attention and concentration. Tntegr. Physiol. Behav. Sci. 34 (1999) p.43-53.

[6] Schroeder, MJ and Barr RE. Quantitative analysis of the electroencephalogram during cranial electrotherapy stimulation. Clin. Neurophysiol. 112 (2001) p. 2075-2083.

DEVICE FOR ACCUPRESURE WORKING IN MAGNETIC FIELD

Sasho Guergov*, Dimiter Dimitrov**, Atanas Dimitrov**

Technical University of Sofia, Faculty of Industrial Technology*, Faculty of Telecommunications**,
1000 Sofia, 8 Kl. Ohridski Blvd

Tel. (+359 2) 965-3246; e-mail: sguergov@tu-sofia.bg

Tel. (+359 2) 965-2278: e-mail: dcd@tu-sofia.bg

Abstract

An acupressure device designed and developed for rotational and axial motion for the treatment of biologically active points. The device is intended to be used in combination with an electromagnetic coil to simultaneously perform magnetic and acupuncture physiotherapy.

1. INTRODUCTION

Acupressure is a massage effect on biologically active points (point massage) or linear action on the meridians and the direction of energy in them (surface massage) [1,2].

Massaging is usually done manually (Fig. 1), with slight pressure and circular motion, making from 50 to 200 movements per minute depending on the location of the point on the various meridians.

Fig.1 Massage technique

Massage points should not be treated either very strongly or very poorly for both treatment and prophylaxis.

In magnetotherapy, the local application of low-frequency magnetic field is the most common [3,4]. This field is excited by inductors that are connected to the magnetotherapy apparatus. This method is used in many diseases. Inductors are most commonly round (toroidal) coils with an opening as shown in Figure 2.

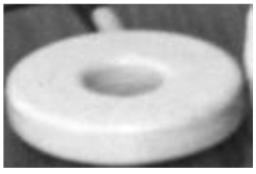

Fig.2 Inductor

If the massaging device can carry massaging movements through the opening of the coil, the two methods of magnetotherapy and acupressure can be combined in simultaneous application. Of course, the inductors should be located above the acupuncture point for the appropriate treatment.

The purpose of this article is to develop and propose acupressure devices that perform simultaneously rotative motion and straight-line motion along with the magnetotherapy procedure. In this way a synergistic effect of the simultaneous effects of both methods will be obtained.

2. BASIC MOVEMENTS AND DEVICE PARAMETERS

Based on the analysis of the main techniques used in the acupressure, it can be seen that the main movements associated with the treatment of the respective points can be reduced to rotational motion, vibration and translational movement (knocking). Furthermore, the thrust pressure on the respective points is in the range of 5 ÷ 15 N. Depending on the location of the meridian point, the thickness of the treated area and the sensitivity of the skin layer, the torque of the device should be within the range of 0.5 ÷ 2.5 Nm.

3. DEVICE STRUCTURE

In the above mentioned prerequisites, a device with rotational-straight-line motion and a maximum torque of 2.5 Nm has been developed.

Figure 3 shows a drawing of the device design. The movable part 8 has a longer length so that the device can be combined with the inductor 9 for the

simultaneous execution of both acupressure and magnetic therapy.

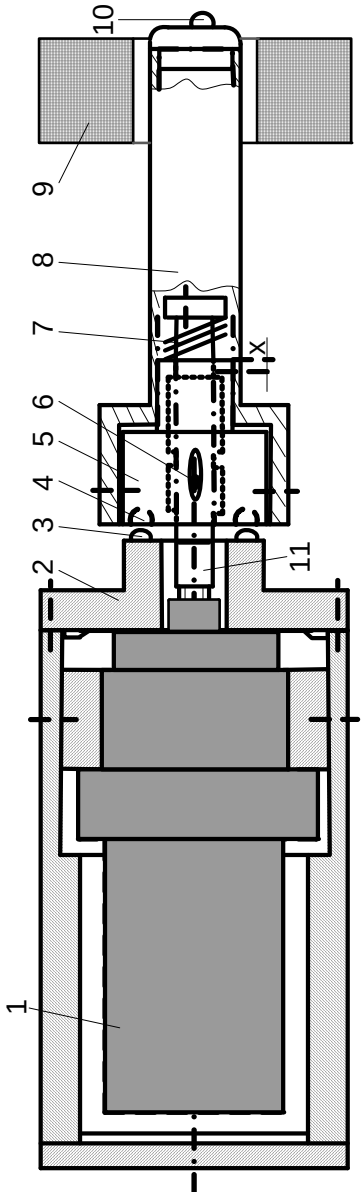

Fig.3 Construction scheme

The rotary motion with frequency of 35 ÷ 150 min-1 on the shaft 11 is obtained from the motor 1 and the sleeve 2 is fixedly attached to the device body. The translational movement (x = 2mm) is obtained by axial displacement of the bush 5 at the hemispherical buts 3 from the holes 4 when the rotary motion is performed. The spring 7 performs a continuous pressure effort between 2 and 5. The number of holes is four, which allowing for four reciprocating movements of the nozzle 8 for one revolution. The torque of the shaft 11 is fed to the movable part 8 by the pin 6.

The massaging butt 10 is eccentrically positioned on the movable part axis, allowing a massaged area around the acupuncture point about 15 mm in diameter.

The stepper motor control system (Fig. 4) consists of a clock generator, a pulse distributor and a driver.

The clock generator is built on the ИС NE555. The impulse distributor consists of D-triggers CD4013, and the final stage is constructed with ULN2804. The maximum supply voltage is 18V, and the current of each phase of the motor is 0.4A. The motor used has 48 steps per turnover. The engine speed changes from 0.5 to 2 turnovers per second, which corresponds to a frequency of steps of 24 to 96 steps per second. This frequency is produced by the clock generator and can be adjusted using the potentiometer R7.

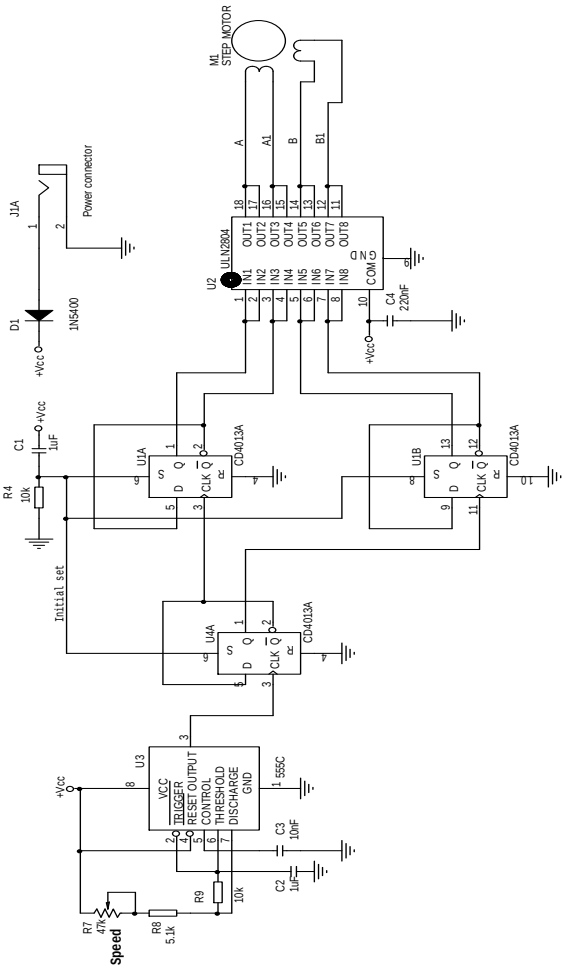

Fig.4 Stepper motor control scheme

Figure 5 shows the device together with the control unit and its application in use.

Fig.5 Acupressure device and application scheme

4. CONCLUSION

A device for acupressure with a torque range of 2.5 Nm, a force of 15 N and a massaging area around the acupuncture point with a diameter of 15 mm has been developed. The design of the devices is consistent with the possibility of simultaneous execution of magnetic therapy. The device has been experimented in real clinical conditions and has demonstrated its ability to work.

References

[1] Hilebreht, M. Acupressure, ISBN 9548793253, Emac, 1998, p. 240

[2] http://zashto-kak.hit.bg/glavnaraze.htm

[3] Guergov, S., Dimitrov, D. System for Therapy with Acupressure and Low Frequency Magnetic Field, 4th International Conference on Communications, Electromagnetics and Medical Applications (CEMA'09), 8th – 10th October, 2009, Sofia, p.75-79

[4] Dimitrov, D., S. Guergov. System for Simultaneously Therapy by Running Low frequency Magnetic Field and Acupressure, 6th International Conference on Communications, Electromagnetics and Medical Applications (CEMA'11), 6th – 8th October, 2011, Sofia, p.48-51.

AUTHOR INDEX